AFRL-AFOSR-JP-TR-2023-0084

Plasticity in High Strength Beta Titanium Alloys

DIPANKAR BANERJEE
SOCIETY FOR INNOVATION AND DEVELOPMENT
INNOVATION CENTRE, INDIAN INSTITUTE OF SCIENCE,
BANGALORE, KARNATAKA, 560012
IND

06/23/2023
Final Technical Report

Air Force Research Laboratory
Air Force Office of Scientific Research
Asian Office of Aerospace Research and Development
Unit 45002, APO AP 96338-5002

REPORT DOCUMENTATION PAGE

PLEASE DO NOT RETURN YOUR FORM TO THE ABOVE ORGANIZATION.

1. REPORT DATE	2. REPORT TYPE	3. DATES COVERED	
20230623	Final	START DATE 20170828	END DATE 20210827

4. TITLE AND SUBTITLE
Plasticity in High Strength Beta Titanium Alloys

5a. CONTRACT NUMBER	5b. GRANT NUMBER	5c. PROGRAM ELEMENT NUMBER
FA2386-17-1-4079		61102F
5d. PROJECT NUMBER	**5e. TASK NUMBER**	**5f. WORK UNIT NUMBER**

6. AUTHOR(S)
Dipankar Banerjee

7. PERFORMING ORGANIZATION NAME(S) AND ADDRESS(ES)
SOCIETY FOR INNOVATION AND DEVELOPMENT
INNOVATION CENTRE, INDIAN INSTITUTE OF SCIENCE,
BANGALORE, KARNATAKA 560012
IND

8. PERFORMING ORGANIZATION REPORT NUMBER

9. SPONSORING/MONITORING AGENCY NAME(S) AND ADDRESS(ES)	10. SPONSOR/MONITOR'S ACRONYM(S)	11. SPONSOR/MONITOR'S REPORT NUMBER(S)
AOARD UNIT 45002 APO AP 96338-5002	AFRL/AFOSR IOA	AFRL-AFOSR-JP-TR-2023-0084

12. DISTRIBUTION/AVAILABILITY STATEMENT
A Distribution Unlimited: PB Public Release

13. SUPPLEMENTARY NOTES

14. ABSTRACT
Plasticity of high strength titanium alloys is influenced by the scale and distribution of intragranular ?. We aim to develop a relationship. between microstructural length scales, microtexture and the mean free path for slip. We also aim to develop a predictive model for yield strength in these materials using crystal plasticity techniques. We have quantitatively determined structural parameters associated with a phase distribution and morphology as a function of heat treatment in the high strength, metastable b alloy Ti 5553. Compression tests had been carried out at room temperature to show the variation of yield strength and work hardening as a function of these structural parameters. Surface slips offsets had been analysed in relation to the scale of the alpha microstructure and it has been shown that slip initiates in the b phase on the {112} <111> system in the form of heterogenous slip bands. Slip lengths are restricted by the interaction of the slip bands with a variants, and therefore depends on the a variant distribution statistics. Yield strength has been shown to scale with slip length and alpha interparticle spacing. Strain partitioning has been examined by both DIC and qualitative EBSD techniques. These experimental results are complemented by crystal plasticity simulations of single beta grains containing alpha variant distributions.

15. SUBJECT TERMS

16. SECURITY CLASSIFICATION OF:			17. LIMITATION OF ABSTRACT	18. NUMBER OF PAGES
a. REPORT	b. ABSTRACT	c. THIS PAGE		
U	U	U	SAR	39

19a. NAME OF RESPONSIBLE PERSON	19b. PHONE NUMBER *(Include area code)*
JEREMY KNOPP	315-227-7006

Standard Form 298 (Rev.5/2020)
Prescribed by ANSI Std. Z39.18

PLASTICITY IN HIGH STRENGTH BETA TITANIUM ALLOYS

FA2386-17-1-4079

Final Report

Dipankar Banerjee
Materials Engineering
Indian Institute of Science
Bangalore 560012
dbanerjee@iisc.ac.in

Executive Summary

- Plasticity of high strength titanium alloys is influenced by the scale and distribution of intragranular α.
- We aim to develop a relationship. between microstructural length scales, microtexture and the mean free path for slip
- We also aim to develop a predictive model for yield strength in these materials using crystal plasticity techniques.
- We have quantitatively determined structural parameters associated with α phase distribution and morphology as a function of heat treatment in the high strength, metastable β alloy Ti 5553.
- Compression tests had been carried out at room temperature to show the variation of yield strength and work hardening as a function of these structural parameters.
- Surface slips offsets had been analysed in relation to the scale of the alpha microstructure and it has been shown that slip initiates in the β phase on the {112} <111> system in the form of heterogenous slip bands. Slip lengths are restricted by the interaction of the slip bands with α variants, and therefore depends on the α variant distribution statistics. Yield strength has been shown to scale with slip length and alpha interparticle spacing.
- Strain partitioning has been examined by both DIC and qualitative EBSD techniques. These experimental results are complemented by crystal plasticity simulations of single β grains containing α variant distributions.

Collaborations and Contributors

1. Prof. Satyam Suwas, Faculty, Materials Engineering, IISc , plasticity analysis

2. Aman Soni, undergraduate student at MNIT, Jaipur and intern at Materials Engineering, IISc, crystal plasticity analysis

2. Prof. Mark de Graef, Metallurgy and Materials Engineering Carnegie Mellon University,qualitative EBSD techniques to determine strain partitioning in fine scale multivariant distributions of α in a β matrix.

3. S.J. Suresha, Research Associate, TEM to determine slip structures in Ti5553.

4. Shanoob Balachandran, former PhD student at Materials Engineering, IISc, on slip length simulations in multivariant α structures.

5. Manaswini Chinara, graduate research assistant, on the effects of structure and slip length on mechanical behaviour in Ti5553.

6. Subham Ray, undergraduate student at NIT Durgapur and summer intern at IISc, on the effect of heat treatment and. on volume fraction of α and related mechanical behaviour in Ti5553.

8. Mainak Sen, Postdoctoral Fellow on quantitative microstructural characterization and heat treatment.

9. Syed Idrees Afzal Jalali, Post Doctoral Fellow, Digital Image Correlation of strain partitioning in aged β structures

10. K.U. Yazar, postdoctoral fellow, crystal plasticity analysis

11. Tejanath Suredddy, graduate research assistant, crystal plasticity analysis

1. Background

We highlight some recent developments in microstructure development and the mechanical behavior in high strength beta titanium alloys. In a recent publication, we have demonstrated that intragranular α variant distribution arising from a direct β to α transformation is strongly biased towards trivariant clusters of variants that share a common close packed direction between the α and β phase [1]. The frequency of occurrence of various trivariant configurations has been experimentally and theoretically assessed. A summary of results is shown in Figure 1.

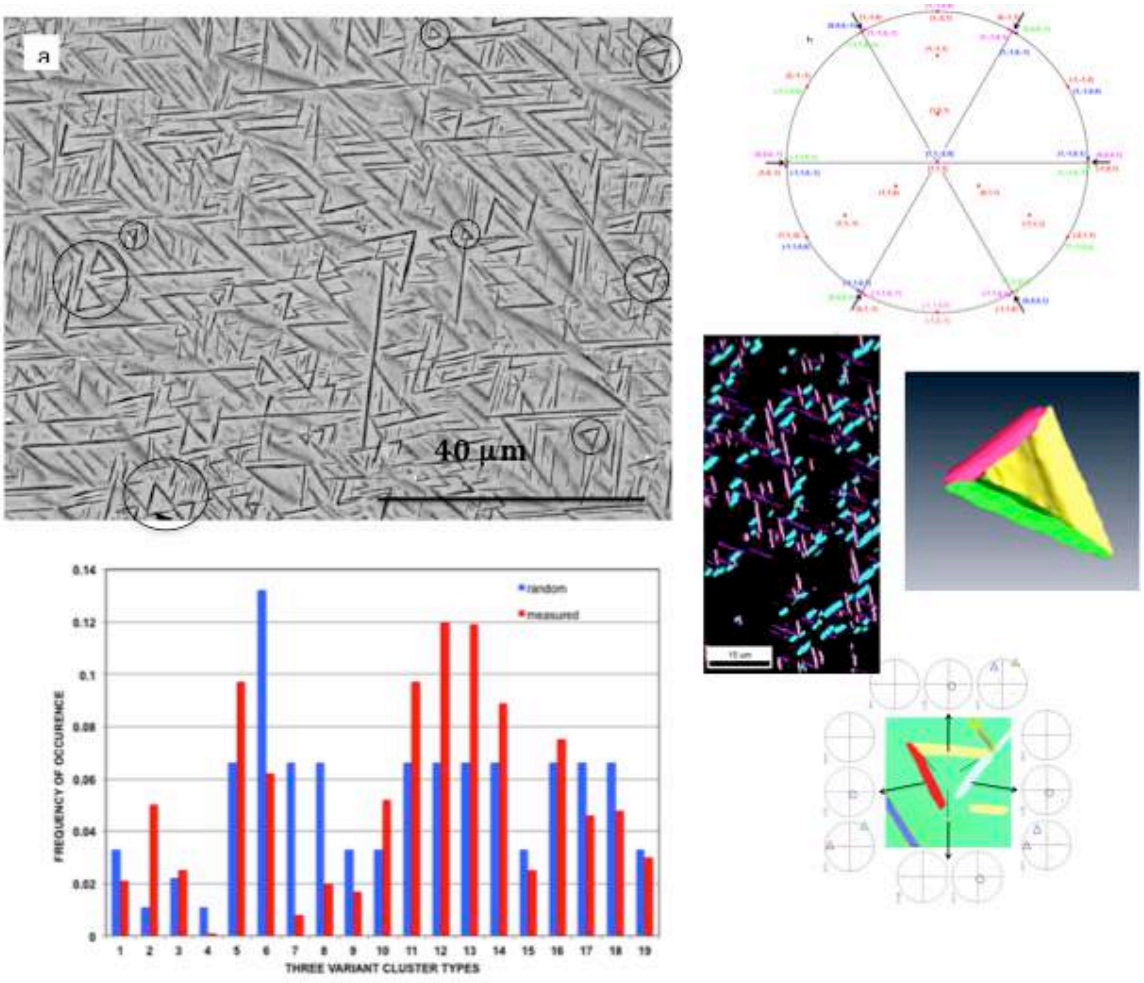

Figure 1: α phase distribution in Ti5553 [1]

In a parallel development [2,3] it has been shown that hyperfine distribution of α can be engineered through transformation pathways that apparently involve intermediary phases such as ω and these result in ultrahigh strengths in these β titanium alloys. It is not clear whether α variant distribution statistics in such apparently mediated transformation to α follow the same pattern as observed by us in the direct β to α transformation, although the appearance of α variant distribution is very similar.

Clearly a detailed analysis of plasticity of such alloys as influenced by the scale and distribution of intragranular α would significantly enhance our understanding of the plasticity of this important class of alloys.

We believe that this will constitute the first such attempt to evolve quantitative models for room temperature plasticity in high strength titanium alloys. Within an ICME context such models provide the opportunity to explore fracture toughness and fatigue models for this class of alloys in the future. In addition, the analysis provides the framework for understanding plasticity in the transformed β segment of bimodal equiaxed α +transformed β structures of titanium alloys. In current crystal plasticity analysis, the properties of the transformed beta segment of the structure are homogenized to representative values.

2. Research Timelines

Based on the approach outlined above, we proposed the following timelines for a 3-year program.

Year One

- Heat treatment employing different transformation pathways to develop α+β structures at different length scales.
- Quantitative analysis of structure and microtexture in the form of variant distribution statistics.
- Principle component analysis to identify reduced order representations of structure.
- Room temperature compression data

Year 2

- Characterization of plasticity through the statistics of slip length from surface offsets for various microstructural scales.
- Identification of dominant slip systems through EBSD analysis and their relation to the global Schmid factor
- This may be supported by DIC for very early stages of plastic deformation to quantify slip intensity
- Transmission electron microscopy of slip, particularly the analysis of β slip system interaction with the 12 variants of the α phase

Year 3

- Data analysis

Year 4

- No cost extension granted in view of work interruptions due to Covid

3. Research Methodology

Our approach has been to define room temperature yield strength and work hardening to small strains in compression as a function of microstructural scale. These different scales will be achieved in a Ti5553 alloy This will constitute the data set that we will attempt to understand and model through various characterization and modeling techniques

Structure

The development of a large data set of α stereology and variant distribution across several β grains will be developed for analysis

Deformation

The crystallography and scale of slip has been determined from surface offsets on electropolished surfaces of compression sample after small strains, Electron microscopy has been used to examine the dependence of slip transfer across α from the β phase as dependent on the crystallography of α variants within a β matrix, The nature of slip transmission will be analyzed with several criteria that have been developed to understand slip transmission across grain boundaries [4]. We have used techniques developed by Prof. Marc De Graef of Carnegie Mellon University in collaborative work with him to examine strain partitioning by EBSD and strain partitioning analysis has also been accomplished by special digital correlation techniques developed for this alloy.

Analysis

The information derived from these studies has been used to derive a relationship between microstructural length scales, variant distribution statistics and slip length. We have then examined whether slip length can be used as a simple predictor of yield. In addition, a more rigorous analysis has been completed using crystal plasticity techniques

4. Results

4.1. Structure

In work carried out anticipating formal sanction, a detailed analysis was carried of structure evolution with aging time in the TI5553 alloy. The alloy samples were heat treated from the as-cast condition for 4.5h, 48h, 96 h and 144 h at 765℃. All samples have a very large β grain size of about 1mm (see Figure 2f). Figure 2 shows microstructure as a function of ageing time. The volume fraction remained essentially constant during over this time period indicating this time range was associated with a coarsening process. The expected 3d shape of the α particles is shown in Figure 3a [1]. Random 2d sections of such particles will appear as ellipses The average major axis and average minor axis of such ellipses vs aging time have been measured from EBSD scans taken in several different grains of each sample using TSL-OIM. The variation of the major axis and minor axis of α particles in these 2d sections are

shown in Figure 4(a) and (b) respectively. The data shows average valued measured in different grains. The orientation of the 2d section of the β grain may be expected to influence the ellipse dimensions as discussed below. However, the scatter observed from grain to grain is not significant. Both the average major axis and the average minor axis increase with time, but the rate of coarsening appears to decrease with time.

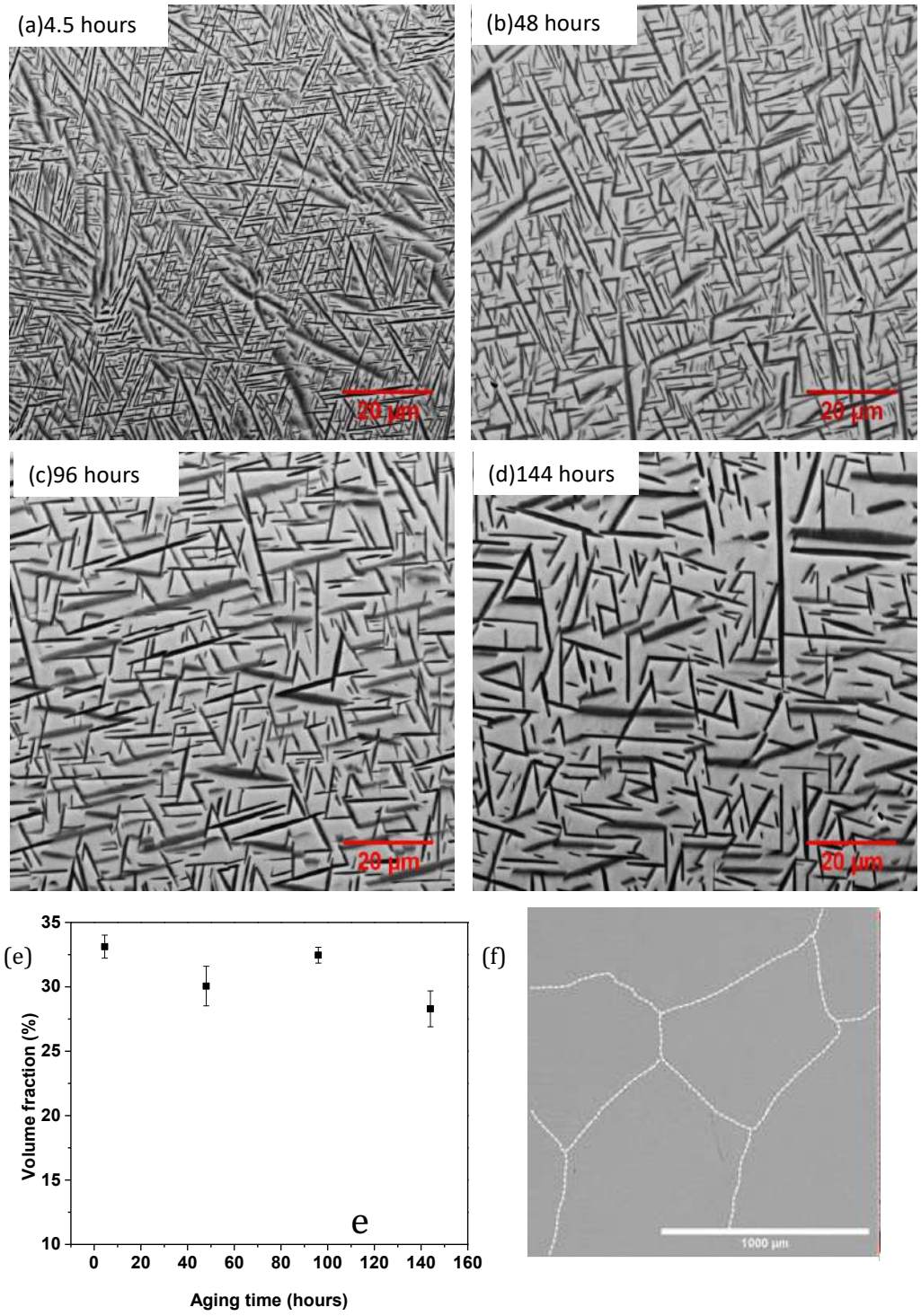

Figure 2: (a-d) the effect of ageing time at 765°C on the scale of α precipitation (e) the volume fraction remains a constant over this time period (f) the β grain size

It would not be appropriate to carry out an analysis of coarsening from the dimensions obtained from such 2d sections since these dimensions do not represent the true dimensions of 3d plates from which such sections are obtained. The only analytical method available to derive 3d data from 2d sections of similar particles is DeHoff's method [5]. This method involves representing the particles as oblate spheroids and assumes that the all possible oblate spheroid orientations exists in the sample. However a careful examination of the particles in appropriate orientations shows that such an assumption of the particle shape is not valid. Thus Figure 3a indicates that the particles are better represented as ellipsoidal discs with 3 dimensions: the major (a) and minor axis (b) of the disc and its thickness (c). Further, such particles are not randomly oriented in the matrix but follow specific orientations as determined by the Burgers orientation relationship. (BOR).

$(0001)\alpha//(110)\beta:<11\bar{2}0>\alpha//<1\bar{1}1>\beta$

According to the Burgers OR, the side face (thickness) of the α-plate is formed by planes $(0001)\alpha \parallel (110)\beta$. The broad face of the α- plate is close to $[1\bar{1}00]\alpha \parallel [112]\beta$ [6]. Thus, projections along [112] can be used to estimate the dimensions a and b. Similarly projections along [110] and [111] directions can be used to determine a, c and b, c respectively a shown in Figure 3b. If the plane of sectioning is perpendicular to any other direction, these dimensions cannot be distinguished. Thus in order to estimate the a, b and c dimensions of the α plates, it is necessary to search for β grains with orientation close to [112], [111] and [110] for each aging time. Figure 3c shows an example of the above method in which the section of the β grain is nearly perpendicular to [110], [111] and [112]. In the [110] orientation, two variants of α exist that have their basal plane normal parallel to this [110] and the OIM has been partitioned to show only these two variants. Both these variants can be used to determine 'c and 'a'. In the [111] orientation , there are 3 variants of α that exist with their $[11\bar{2}0]$ axis parallel to this [111] from which 'b' and 'c' can be determined. The OIM image has been partitioned to show these variants. In the [112] β orientation, only one variant exists parallel to a given [112] and image has been partitioned to show this variant. In the [110] and [111] orientations, the thickness 'c' of the disc will not depend on the position of the sectioning plane with respect to the plate plane as it cuts the precipitate. However the dimension of 'a' and 'b' will be affected by the position of the sectioning plane as is obvious from an examination of Fig. 2b. We are currently examining variations of Saltykov's method [7] for determination of the size distribution of spherical particles from measurement made on plane section to examine whether the true 'a' and 'b' dimensions in 3D can be obtained. Figure 4c shows the plot of a, b and c dimensions of the alpha plate as a function of aging time on which the average major axis and average minor axis measured from EBSD data are superimposed. It is noted that finding sections that are perpendicular to these directions is quite fortuitous and therefore such data could not be obtained for all aging times. The data suggests that the thickness 'c' is well represented by the minor axis in the random 2d sections. Figure 4d shows the average interparticle spacing as a function of time. The average interparticle spacing decreases with increase in aging time. This data has been provided since the variation of yield stress with aging time in the following section has been assessed against this data.

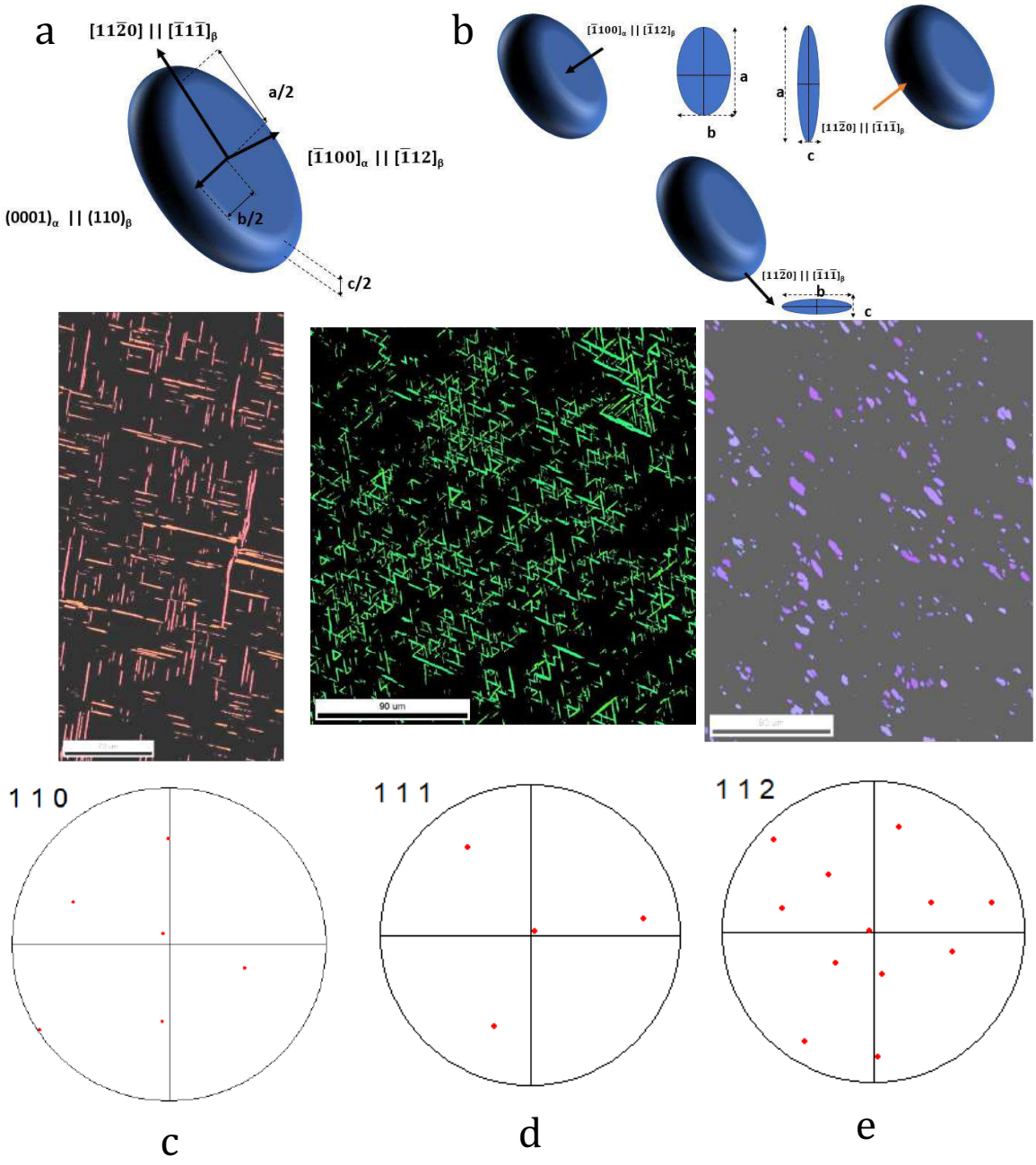

Figure 3: (a) the shape and crystallography of the alpha precipitate the effect (b) the 2d shape of the precipitate in sectioning planes perpendicular to the arrows (c) partitioned EBSD images showing the observed variants along the {110] , [111] and [112] directions as shown in the stereographic projections. The partitioning includes all variants that are observed with the pole along the direction of projection.

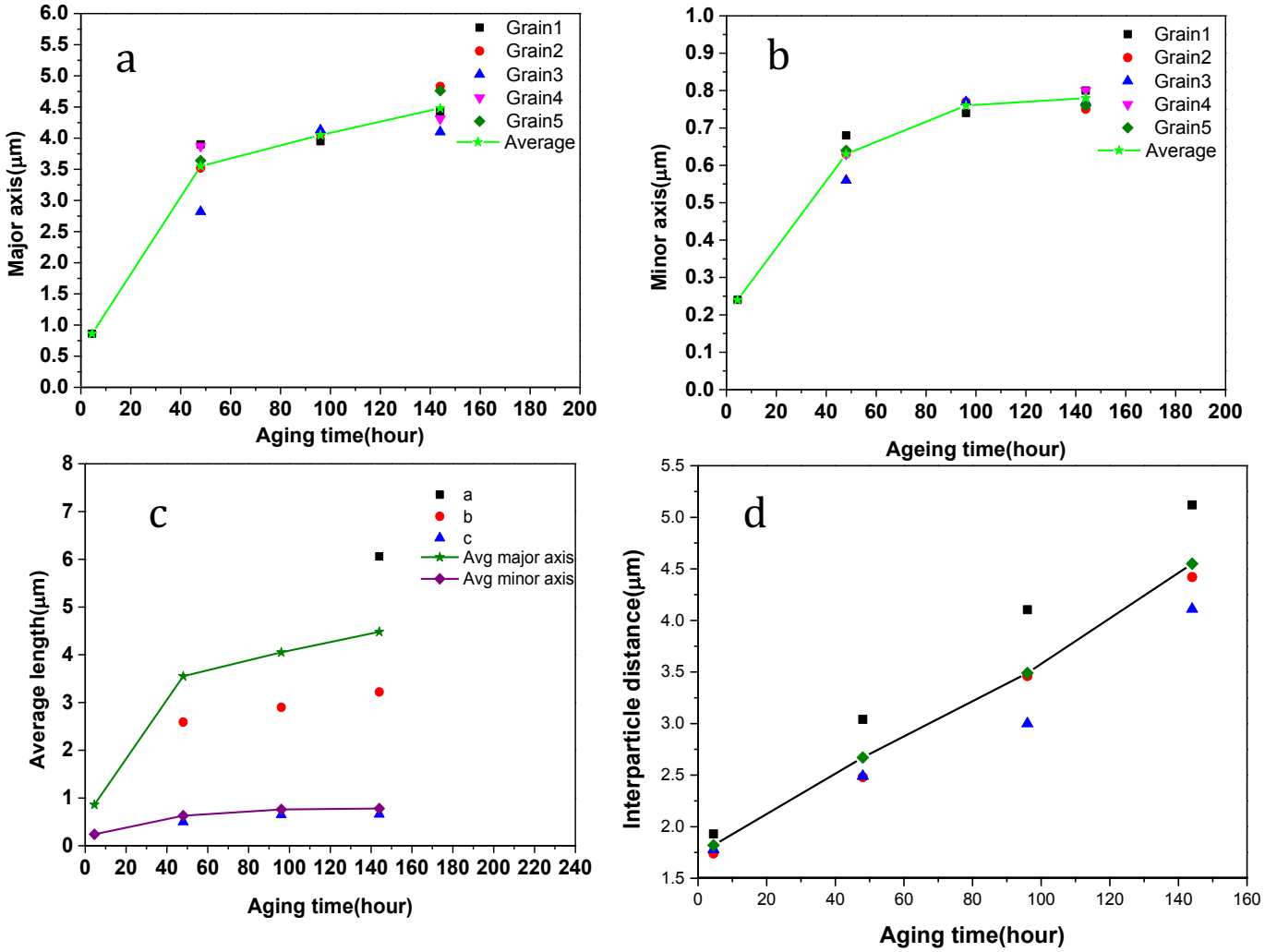

Figure 4: (a) and (b) show the average major and minor axis respectively measured using EBSD TSL software in different grains as a function of aging time. (c) shows the average a, b and c axes measured along the specific orientations in Figure 2 compared to the average major and minor axis (d) the α interparticle spacing as a function of aging time.

Figure 5 shows microstructure of samples heat treated at different aging temperatures to change the volume fraction of α phase and the associated change in the interparticle spacing of the α phase.

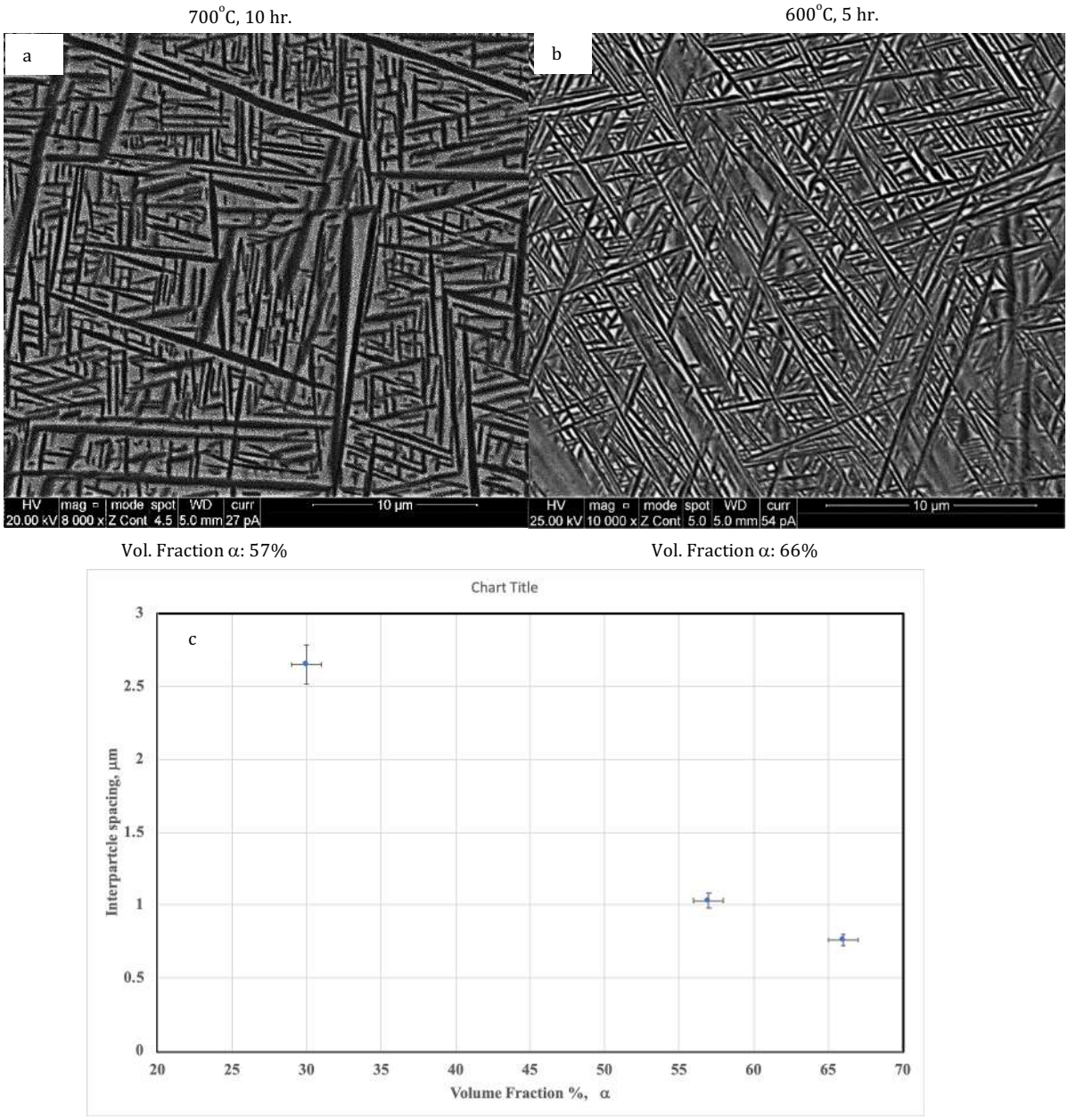

Figure 5: (a) and (b) show variation in microstructure (c) shows variation in α interparticle spacing with volume fraction

4.2. Mechanical Behaviour

Figure 6 shows the variation of yield and work hardening in compression as a function of ageing time at 765°C. As may be expected the yield stress decreases as the microstructure coarsens with ageing time. The work hardening shows a substantial decrease as the microstructure coarsens. Figure 7 shows the effect of changing the volume fraction of α phase on compression yield behaviour. Surface slip offsets were examined after 2% plastic strain by on surfaces electropolished prior to deformation. Figure 8 shows trends as a function of aging time. Planar slip bands are seen. Slip length was examined as a function of aging time and is also shown in Figure 8e. Figure 8 f relates yield strength to slip length and interparticle distance of the α phase in Hall-Petch plots.

Details of slip band interaction between the alpha and beta phases are shown in Figure 9. Figure 9a indicates that slip bands initiate in the β phase and often occur in clusters. Intense slip bands are often observed at α/β interfaces (Figure 9b) Slip band in β can either shear α plates or be blocked by them (Figure 9 c,d). Slip lengths are restricted by blocking at α/β interfaces at certain variants. Single surface trace analysis of slip offsets by EBSD suggested that the operative slip system in β is {112} <111>. Transmission electron microscopy was used to examine slip structure in more detail. Figure 9e shows {112}<111> slip in β shearing α while in Figure9f the same slip system terminates at the α plate.

Figure 10 shows that for a particular set of the {112} <111> β slip system family, slip planes and directions in the twelve variants of the α phase will lie close to the β slip system in only a few cases and Luster-Morris parameters, m′ [8] has been determined in each of these cases, defined by the product of the cosine of the angles between slip plane normal and slip directions between the α and β phases for each α variant . The slip length will then be defined by the non-random distribution of the α variants (Figure 1 and reference [1]) and the probability of slip bands in β intersecting variants across which slip transfer can or will not occur. Simulation of slip lengths for a given variant distribution has been attempted in the following manner. An EBSD scan of the structure is loaded into Matlab with all the crystallography of all variants incorporated. Slip is allowed to initiate in the β phase, in the form of slip lines parallel to the trace of a given {112}<111> slip system and intersect α variants in the path of the slip line. The slip line is terminated at α variant if the m′ parameter is below a certain threshold value. Figure 11a shows these simulated slip lines. The distribution of slip lengths as measured from the Matlab program is shown in comparison with the distribution of slip lengths which are experimentally measured from surface offsets for this ageing treatment. A good match is obtained between the simulation and the experimentally measured distribution, as shown in Figure 11b. Figure 12 shows the changing nature of slip with increasing α volume fraction. A significant localisation with very large shear offsets along α/β interfaces is observed on aging at 600ºC.

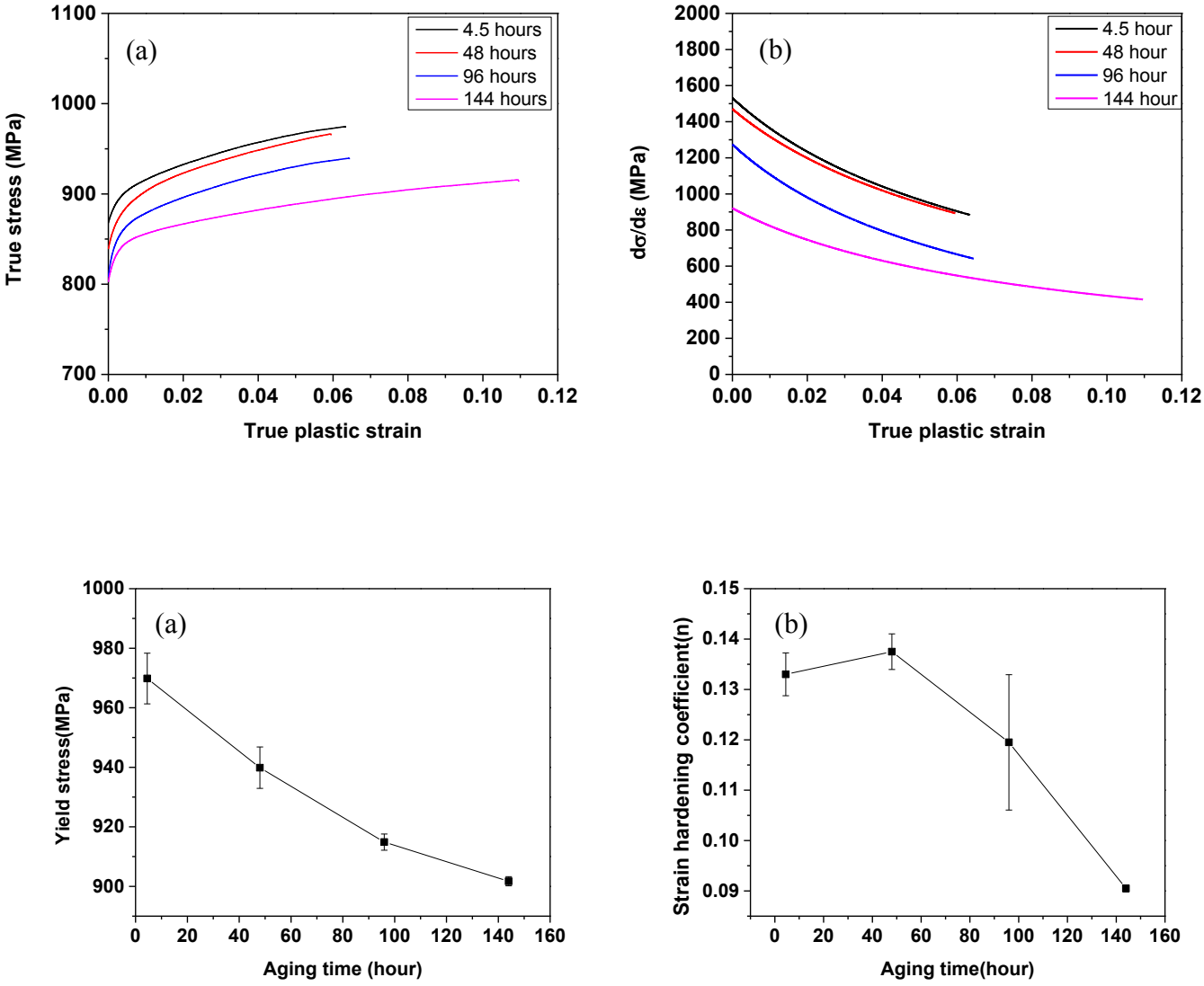

Figure 6: Mechanical behaviour as a function of aging time at 765°C (a) stress-strain curves (b) work hardening (c) yield strength (d) strain hardening coefficient

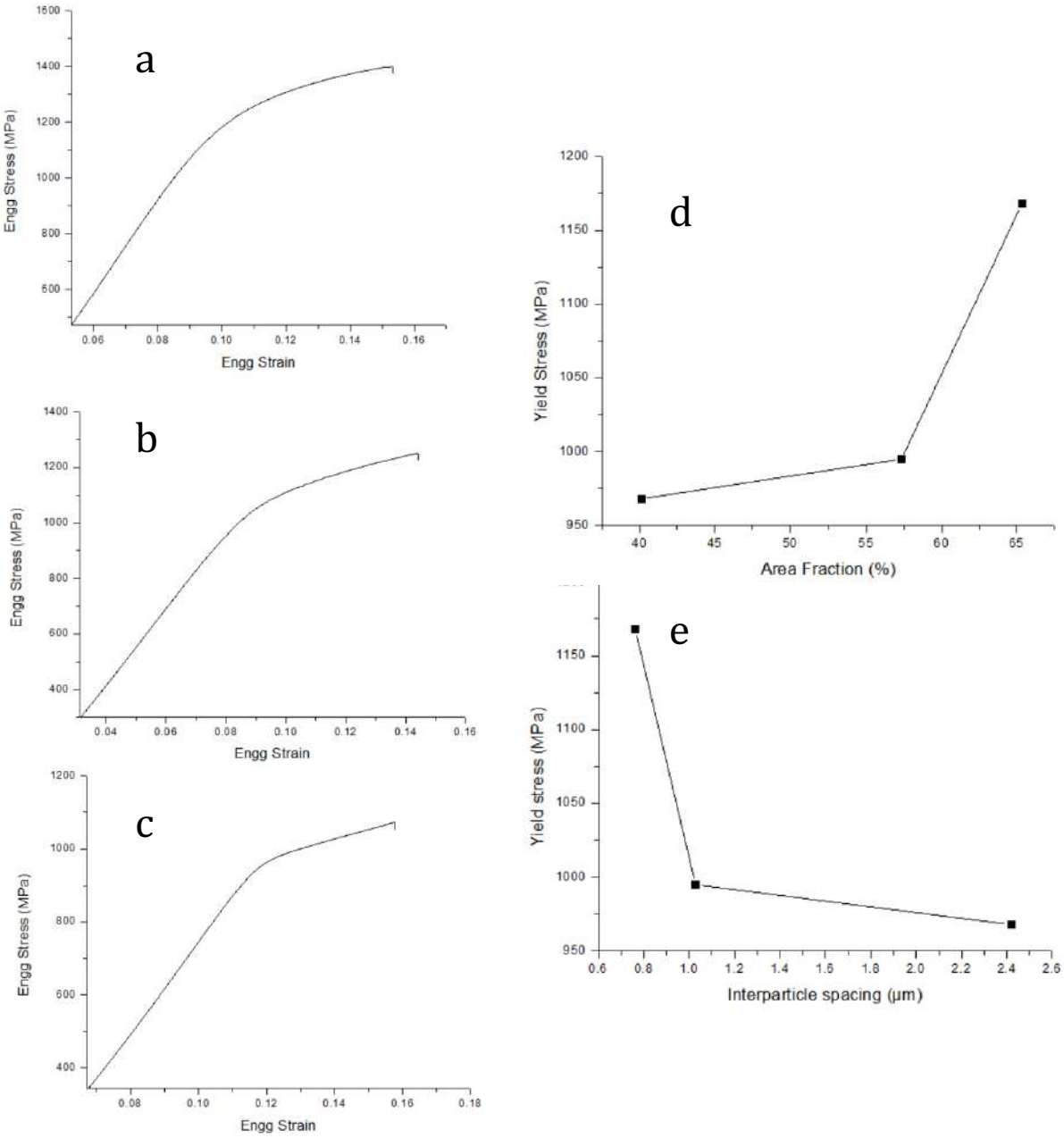

Figure 7: Mechanical behaviour with varying volume fraction of α obtained by varying aging temperature as shown in Figure 5. (a)–(c) engineering stress-strain curves for heat treatments at 760C, 700C and 600C and (d) yield strength vs volume fraction of α (e) yield strength vs interparticle spacing of α.

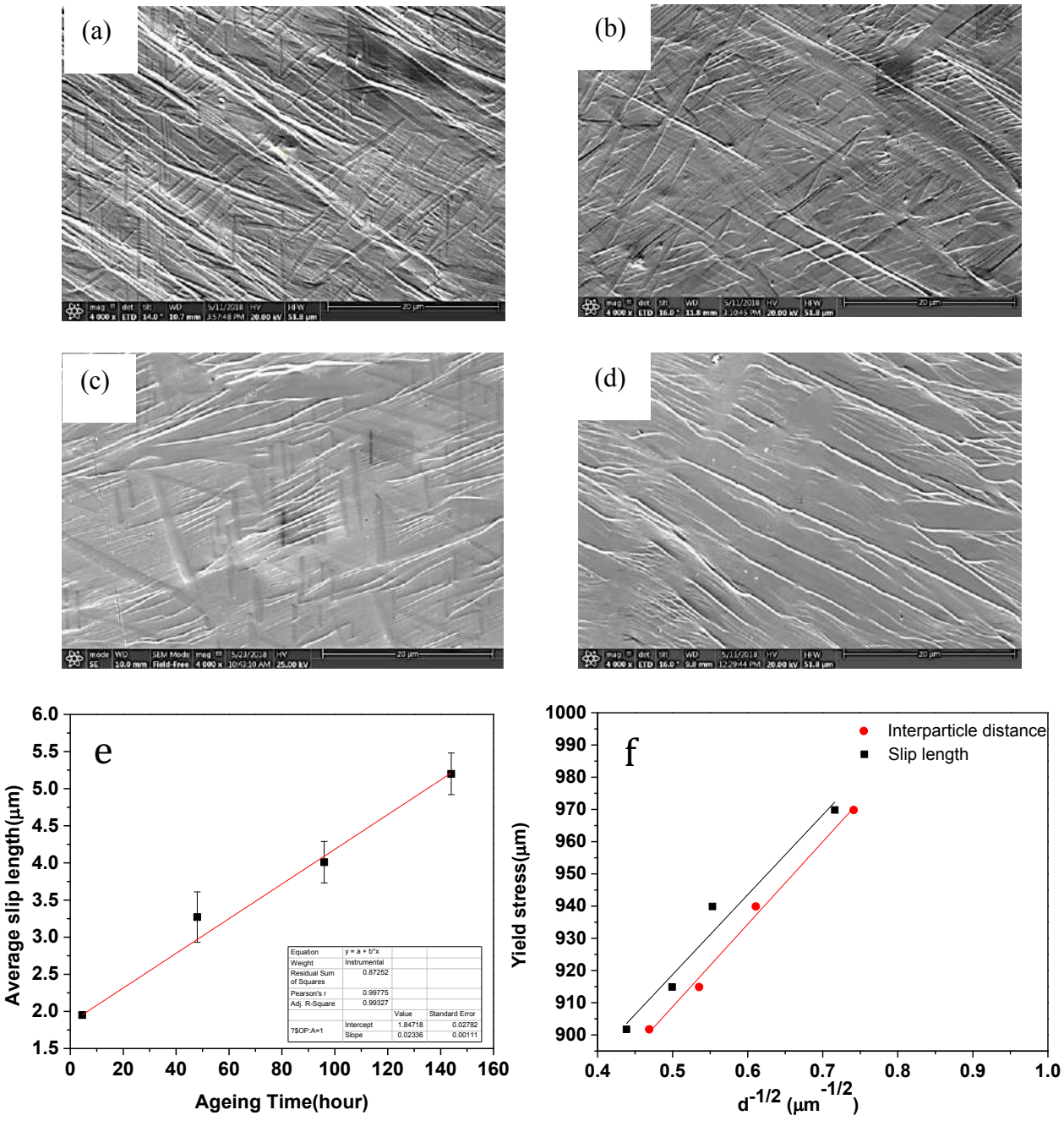

Figure 8: (a)-(d) Surface slip offsets as a function of aging time at 765°C (e) average slip length offsets as a function of aging time at 765°C (f) yield strength in Hall Petch plot with interparticle distance and slip length

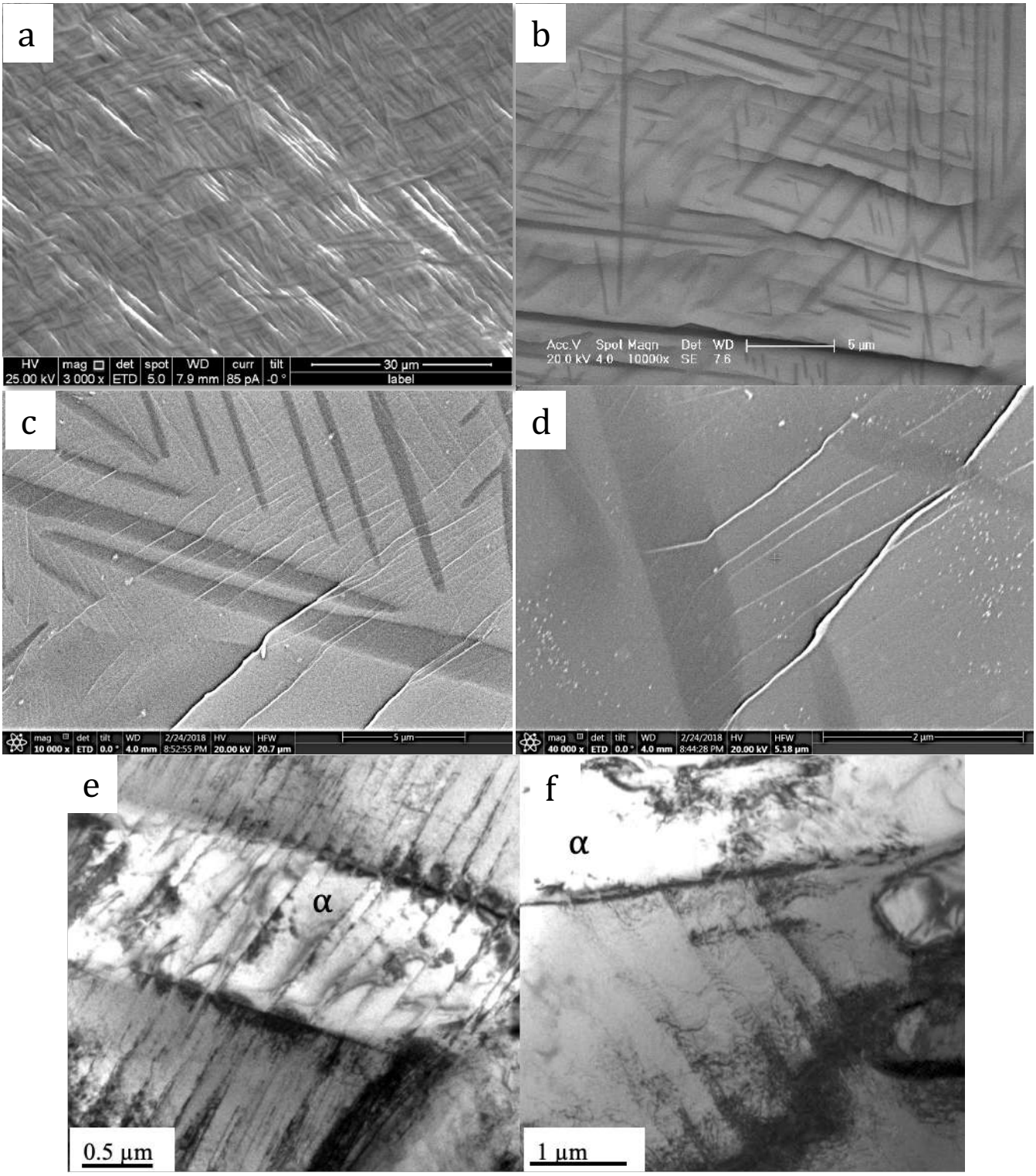

Figure 9: (a)-(d) Surface slip offsets after aging at 144 hr at time at 765^{o}C at different magnifications (e) α plate sheared by a slip band in β (f) slip band in β blocked by an α plate.

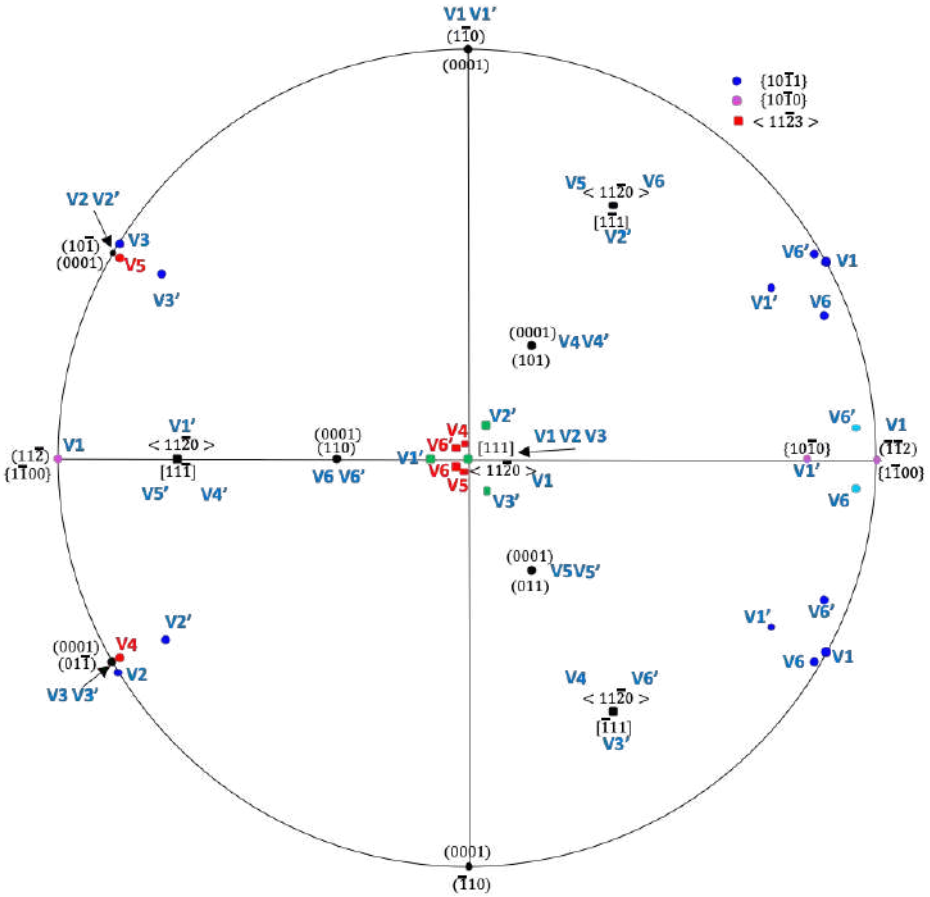

	Variant		α Slip plane	α Slip direction	θ	ϕ	m
V1	(1-10) //(0001)	[111]//[11$\bar{2}$0]	{10$\bar{1}$0}	<11$\bar{2}$0>	0	0	1.000
			{10$\bar{1}$1}	<11$\bar{2}$0>	28	0	0.883
			{10$\bar{1}$1}	<11$\bar{2}$0>	28	0	0.883
V1'	(1-10) //(0001)	[11$\bar{1}$]// [11$\bar{2}$0]	{10$\bar{1}$0}	<11$\bar{2}$0>	10	10	0.970
			{10$\bar{1}$1}	<11$\bar{2}$0>	30	10	0.853
			{10$\bar{1}$1}	<11$\bar{2}$0>	30	10	0.853
V2	(10-1) //(0001)	[$\bar{1}$1$\bar{1}$}//[11$\bar{2}$0]	(0001)	<11$\bar{2}$0>	30	0	0.866
			{10$\bar{1}$1}	<11$\bar{2}$0>	32	0	0.848
V2′	(10-1) //(0001)	[111}//[11$\bar{2}$0]	(0001)	<11$\bar{2}$0>	30	10	0.853
			{10$\bar{1}$1}	<11$\bar{2}$0>	32	10	0.835
V3	(01-1) //(0001)	[111}//[11$\bar{2}$0]	(0001)	<11$\bar{2}$0>	30	0	0.866
			{10$\bar{1}$1}	<11$\bar{2}$0>	32	0	0.848
V3′	(01-1) //(0001)	[$\bar{1}$11}//[11$\bar{2}$0]	(0001)	<11$\bar{2}$0>	30	10	0.853
			{10$\bar{1}$1}	<11$\bar{2}$0>	32	10	0.835
V4	(101) //(0001)	[$\bar{1}$11}//[11$\bar{2}$0]	{10$\bar{1}$1}	<11$\bar{2}$3>	30	4	0.864
V4′	(101) //(0001)	[11$\bar{1}$}//[11$\bar{2}$0]					
V5	(101) //(0001)	[11$\bar{1}$}//[11$\bar{2}$0]	{10$\bar{1}$1}	<11$\bar{2}$3>	30	4	0.864
V5′	(011) //(0001)	[1$\bar{1}$1}//[11$\bar{2}$0]					
V6	(110) //(0001)	[1$\bar{1}$}//[11$\bar{2}$0]	{10$\bar{1}$1}	<11$\bar{2}$3>	30	4	0.864
			{10$\bar{1}$1}	<11$\bar{2}$3>	22	4	0.925
			{11$\bar{2}$2}	<11$\bar{2}$3>	3	4	0.996
V6′	(110) //(0001)	[$\bar{1}$11}//[11$\bar{2}$0]	{10$\bar{1}$1}	<11$\bar{2}$3>	30	4	0.864
			{10$\bar{1}$1}	<11$\bar{2}$3>	22	4	0.925
			{11$\bar{2}$2}	<11$\bar{2}$3>	3	4	0.996

The specific β slip plane and direction considered to determine m′ is (11$\bar{2}$) [111]

Figure 10: The stereographic projection shows the closest slip planes and directions in 12 variants of the α phase to a single (11$\bar{2}$) [111] slip plane in β. The m′ parameter for these slip systems is provided in the table.

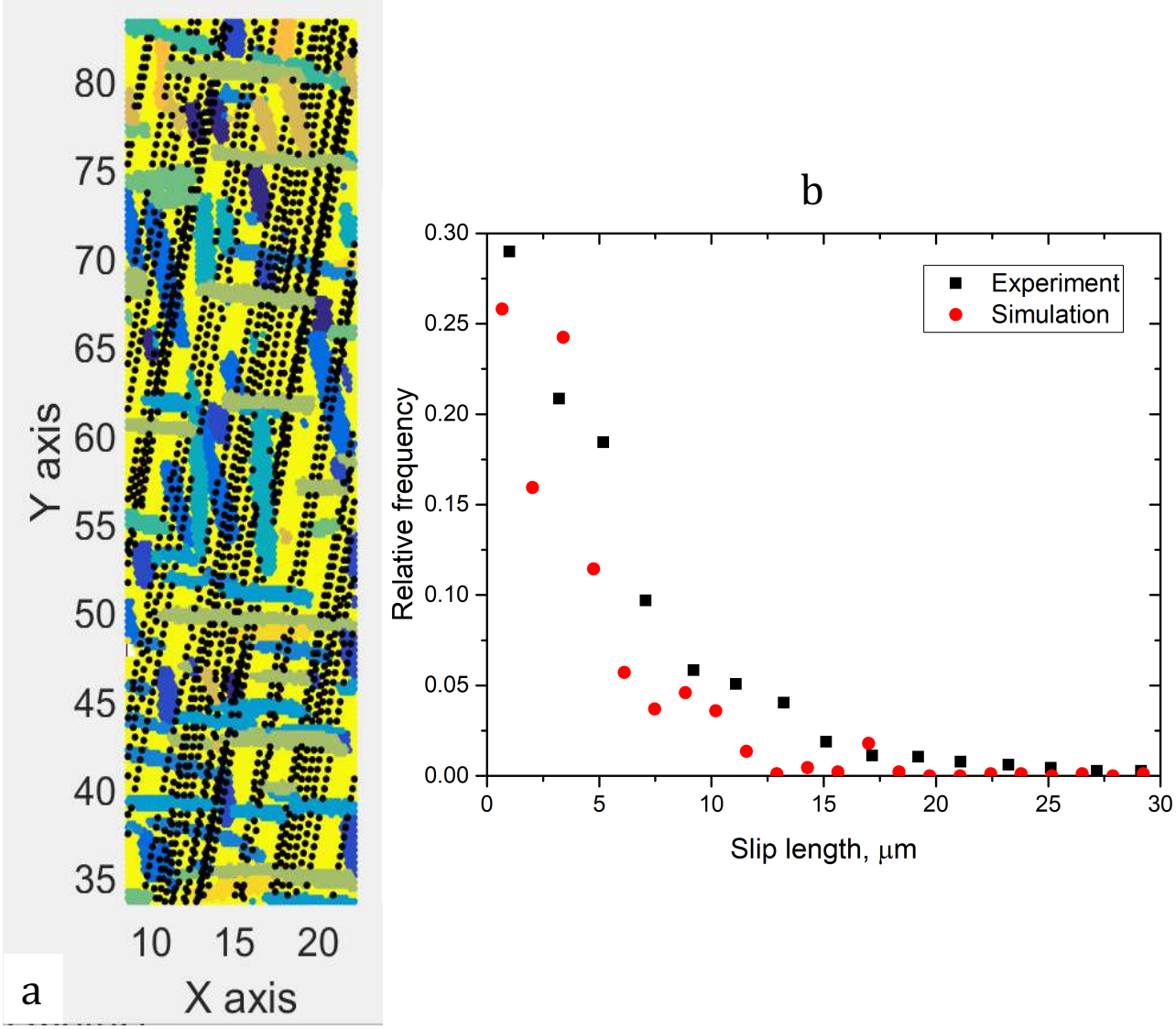

Figure 11: (a) Simulation of slip lengths in a MATLAB program for experimental variant distributions after aging at 144 hours at 765°C. Slip lengths are terminated at an α plate when the m′ value is below threshold number (b) the distribution of slip lengths measured from the simulation compared with experimentally measured distributions.

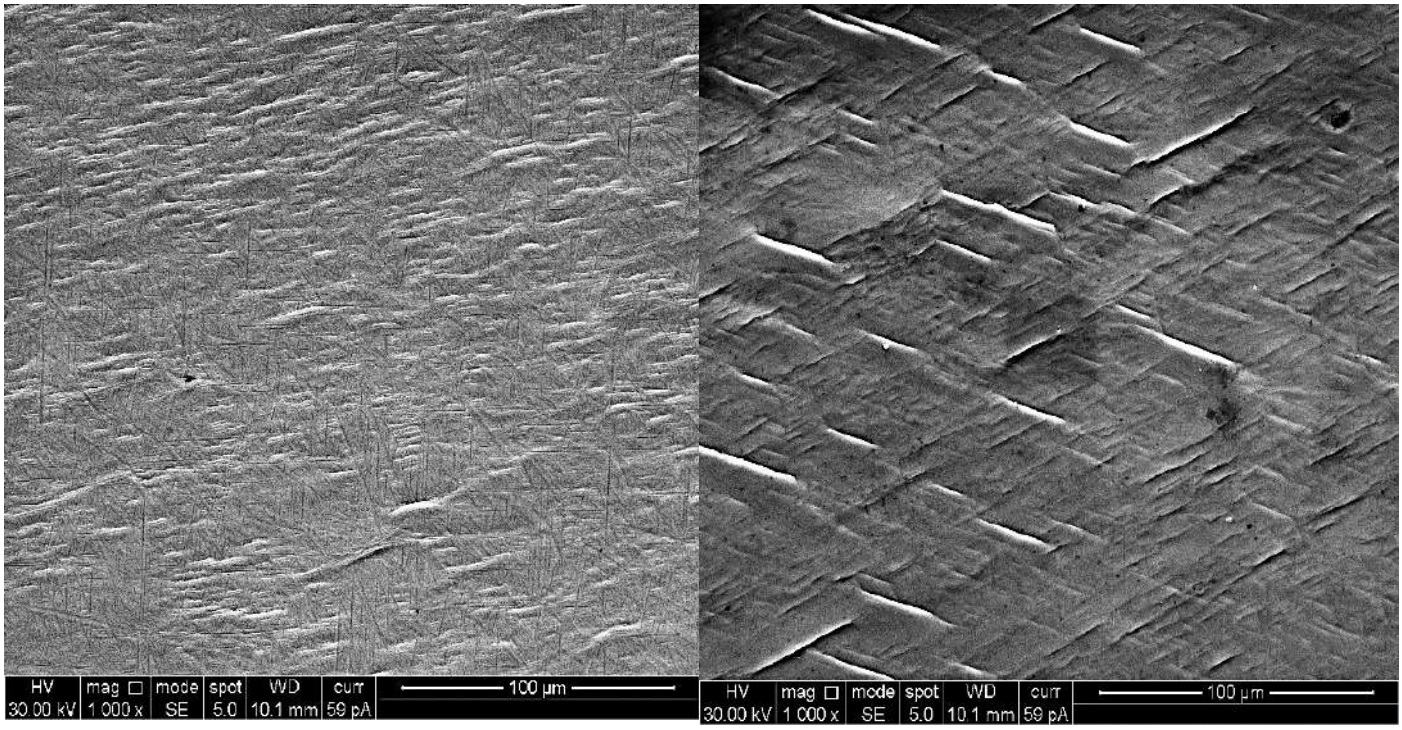

Figure 12: Surface slip offsets with (a) 57% α and (b) 65% α.

4.3. Strain partitioning

We have attempted to measure strain partitioning between the alpha and beta phases using digital image correlation, as well as a qualitative techniques based on EBSD. These data were compared with strain partitioning assessed by crystal plasticity techniques using the Damask software provided to us by Philip Eisenlohr of Michigan Technical University. Figure 13 illustrates our initial attempts to establish strain partitioning by digital image correlation. The speckle pattern shown in Figure 13a was incorporated by a Pt deposit in a dual beam FIB. Attempts to produce a finer scale of pattern were not successful. The number of contrast points across the thickness pf the α grain is only 2-3. The plastic strain partitioning shown in Figure 13b does illustrate the heterogeneity in strain that develops . An alternative method that was evaluated during the visit of Prof. Marc de Graef of Carnegie Mellon University to our department was to use a high resolution EBSD technique to qualitatively evaluate strain partitioning these fine scale structures. Without going into the explicit detail of the technique, a measure of similarity in orientation is computed for each pixel in the EBSD pattern to the ideal orientation in a dictionary matching technique for the undeformed and deformed structures. The deviation of this orientation similarity measure in a histogram plot indicates qualitatively the strain level. A typical result is shown in Figure 14. The results show the strong strain partitioning to and heterogeneities in strain in the β phase and also the strain differences in individual variants of the α phase. Nevertheless, this is a qualitative method at this time.

Finally nanoscale patterning techniques has been developed which meets with the requirements of DIC analysis on these fine scale structures. This technique has been complemented by a coarser paint based speckle distribution. Optical DIC was employed for macro DIC on one face of the cuboidal sample with an area of ~ 12 mm^2. A black on white acrylic paint was sprayed on Ti5553 aged at 700 ^oC for 144 hours (700-144 with α volume fraction of 44% and mean α thickness of 1.2 μm and α lath spacing of 1.9μm) with an airbrush at 20 PSI air pressure. The resultant pattern, shown in Figure 15a, offers a resolution of ~100 mm which is appropriate for strain distribution at the scale of the β grains and also for the average strain in the whole sample. The optical DIC was performed using a Canon DSLR with a 55 mm macro lens, and the image sequence was analyzed using VIC[1]-DIC software. Due to the localized nature of α plate distribution, the strain at the scale of α-β microstructure was analyzed by adapting micro-DIC techniques. A modified Kammer's and Daly [9] method was employed to deposit Au nanoparticles on the surface of Ti to enable SEM based correlation for strain. First, the surface of well-polished Ti samples (with the same size as for macro DIC) was hydroxylated by UV light exposure for 4-5 hours [10]. Following this, the samples were ultrasonicated in distilled H2O, creating an abundance of -OH groups on the surface. Subsequently, the samples are dipped in a 1:5, methanol: 3-mercaptopropyl methyl dimethoxysilane (MPMDMS) for 24 hours. This is an organosilane that acts as a binder between the Au nanoparticles and the -OH group at the Ti surface. Finally, after a brief ultrasonication in methanol for 1 hour, the MPMDMS layered Ti specimen is dipped in 0.4 millimolar citrate stabilized Au nanoparticle solution for another 24 hours. The MPMDMS binds with -OH groups and acts as preferential sites for Au nanoparticle attachment [10] using primary bonds. This

[1] VIC-2D is a commercial software by Correlation Inc. USA used for two-dimensional strain mapping.

impacts strain correlation in micro DIC in that the primary bonds allow the Au particles to accurately translate the strain from underlying Ti without any pattern fallout during deformation or other artefacts from adhesion-based techniques of pattern binding (which result in inadequate strain translation from sample to pattern, and in some case loss of correlation as well). These steps are schematically shown in Figure 15b. The resultant distribution of Au nanoparticles on Ti is shown in Figure 15b, along with the intensity profile in the area of interest. The displacement resolution in DIC is estimated to be around 50-80 nanometres. This allows for nanometre scale subsets for analyzing the strain in individual α, β phases. This Au distribution density ensures about 12 to 20 Au particles per α grain, equivalent to 5 to 7 strain measurements within one a grain. This is assumed to be optimal for understanding the strain partitioning in this system.

After laying the micro-DIC pattern, the area of interest was imaged on FEI Helios G3 with the imaging conditions of 5 KV and 0.2 nA. The image size was chosen as 2048x1908 pixels. This allows for around 50 x 50 pixels for a 100 x 100 nanometer subset (at 4 contrast points (N) per subset). The number of pixels for good correlation should be > 2(2N +1) [15]). The Ti specimens were tested in compression following the patterning for macro and micro scale DIC. Two compression tests on 700-144 specimens were performed. One was used for macro-DIC and one for micro-DIC. The average strain data from macro-DIC and from loading rod displacement in Figure 16 shows the machine compliance effects for a typical sample. The Youngs modulus obtained from average strain data in macro-DIC (~ 90GPa) is very close to the values reported in the literature [16].

Strain maps were obtained from the macro-DIC tests with a sequence of images at a frame rate of 1frame per second. The time-lapse images were analyzed using VIC-2D software. The resultant strain map obtained from this analysis for 2% global plastic strain is shown in Figure 17a. A strong localization in the strain field (marked by the red region in the figure was observed. Additionally, EBSD analysis was performed to correlate the region of localized strain with the β grain orientations. Schmidt factors and effective stiffness in the loading direction for the β grains are shown in Figure 17 b-d. The b phase is elastically anisotropic and stiffnesses within these grains vary from 23 GPa to 46 GPa, as indicated in Figure 4(I)d for the sample 700-144. The Schmid factor distribution is shown in Figure 4(I)c, and the values given are the maximum values in each grain for either {110} and {112} slip. Significantly larger strains are seen in grain 3 with a low stiffness in the loading direction and a high Schmid factor. In contrast, particularly low strains are associated with grains 6,7 and 8 which have higher stiffness and relatively low Schmid factors. It is possible that surfaces may have played a role in the high strains observed in grain 8, with strain developing from the surface and extending into the sample at roughly 45° to the load axis. Surface effects are again apparent. In this discussion, we have not considered the effect of the underlying α distribution or subsurface grains.

The micro DIC permitted analysis of stress and strain partitioning between β and α within a single β grain. Only one b grain was analyzed in this study to demonstrate the efficacy of the DIC technique in evaluating strain partitioning between phases. The patterns before and after testing were analyzed by nCorr software. Figure 18 shows the average strain measured within the α and β phases as a function of the subset size used in calculating the strain. The average strain measured in the β phase is not a strong function of the subset size, but that of tα increases with subset size below 500nm, which

is about half the average thickness of the alpha laths. While we do not understand the origin of this effect currently, it is possible that using subset sizes of the order of the α thickness results in an incorrect assessment of strain due to discontinuities at the α/β interface**.** We have employed a subset size of 100 nm in estimating the local strain partitioning between the α and β phases. The data indicates higher average strains in β than in α, indicating that slip occurs at lower resolved shear stress in the β phase at the structural scale being evaluated. The average plastic strain in the β phase is 1.8%, while the average plastic strain in α phase is 1.3 % Clearly the β phase is the plastically weaker of the two phases in this alloy and microstructural scale.

Strain partitioning between the α and β phases is shown in Figure 19. The BSE micrograph of the area of interest and the corresponding orientation maps are shown in Figures 19 a and b. The analyzed region has 8 different α orientations out of 12 possible variants. The specific variants are numbered on the pole figure and the orientation image. This area of interest corresponds to grain 5 in Figure 17 The Schmid factors for different slip systems in the α variants and their stiffness in the loading direction is shown in Figures 19 c and d. The maps showing strain partitioning are shown in Figure 19f and within the α variants in Figure 19g. The loading direction is indicated in the micrograph by red arrows (Figure 19 a). The Schmidt factors for β <110> <111> and {112}<111> slip show a very large number of slip systems in each family with Schmid factors greater than 0.4 in these grains, that is, the deformation in β phase is expected to be isotropic in the orientations examined. The stiffness of the β phase in the loading direction is 53 GPa, while the α variants have stiffnesses in range of 80-100 MPa. Strain gradients exist in the β phase, with local regions of higher strain in two distinct locations. Higher strain accumulation is seen in regions (encircled in white) that are remote from the α phase, suggesting that the presence of the stronger a constrains plasticity in β. However, higher strain is also seen in regions associated with the tips of the α laths (encircled in black), indicating that there might exist areas of stress concentration in these regions. Strain in the α phase varies between variants quite significantly. Variant 4 has the highest stiffness and low Schmid factors for 'a' slip (< 0.1) because its c-axis is nearly parallel to the loading direction. It is expected that the CRSS for pyramidal 'c+a' slip will be significantly higher than for 'a' slip. Consequently, strain within this variant is extremely low. Surprisingly, the strain within variant 8 is also very low. This variant has low Schmid factors for prismatic 'a' slip (0.23) and pyramidal 'c+a'; slip, but high Schmid factors for basal and pyramidal 'a' slip. This suggests that the CRSS for basal slip is higher in the α composition of this alloy. Variants 1, 2 and 6 have intermediate strain levels and high Schmid factors for pyramidal and prismatic 'a' slip. Variants 3 and 5 show higher strain levels but also strain gradients within the particles. Comparison with strain within β suggests the strain levels within these variants reflect slip transfer from β to a rather than the global Schmid factor.

This study was extended to insitu testing in an SEM using microtensile tests. The geometry of these tests is shown in Figure 20. The use of microtensile samples permitted the examination of strain partitioning within single beta grains (single crystal of β with α precipitates because of the large β grain size. The heat treatments chosen were 765 ^{o}C for 48 hours and 600 ^{o}C for 6 hours to examine the effect of α volume fraction. The resulting microstructures and strain partitioning is shown in Figure

21. the β phase accumulates higher strain at lower α volume fractions corresponding to the higher heat treatment temperature. At higher α volume fraction the α phase has a higher strain (albeit orientation dependent). The related stress-strain curves are shown in Figure 22. The strain partitioning seems to reflect in the work softening when β accumulates higher strain.

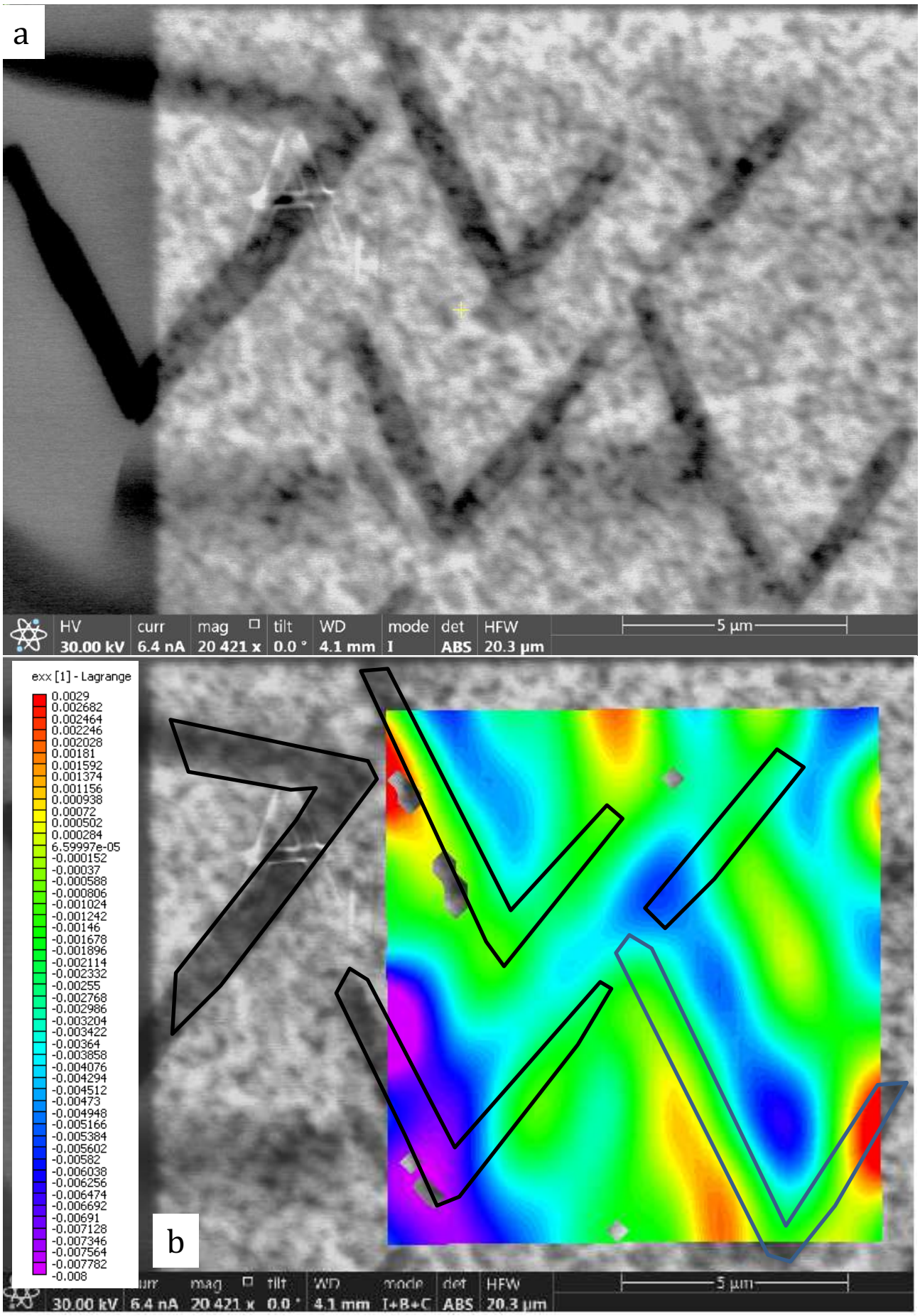

Figure 13: (a) FIB deposited Pt speckle (b) strain distribution superimposed on structure

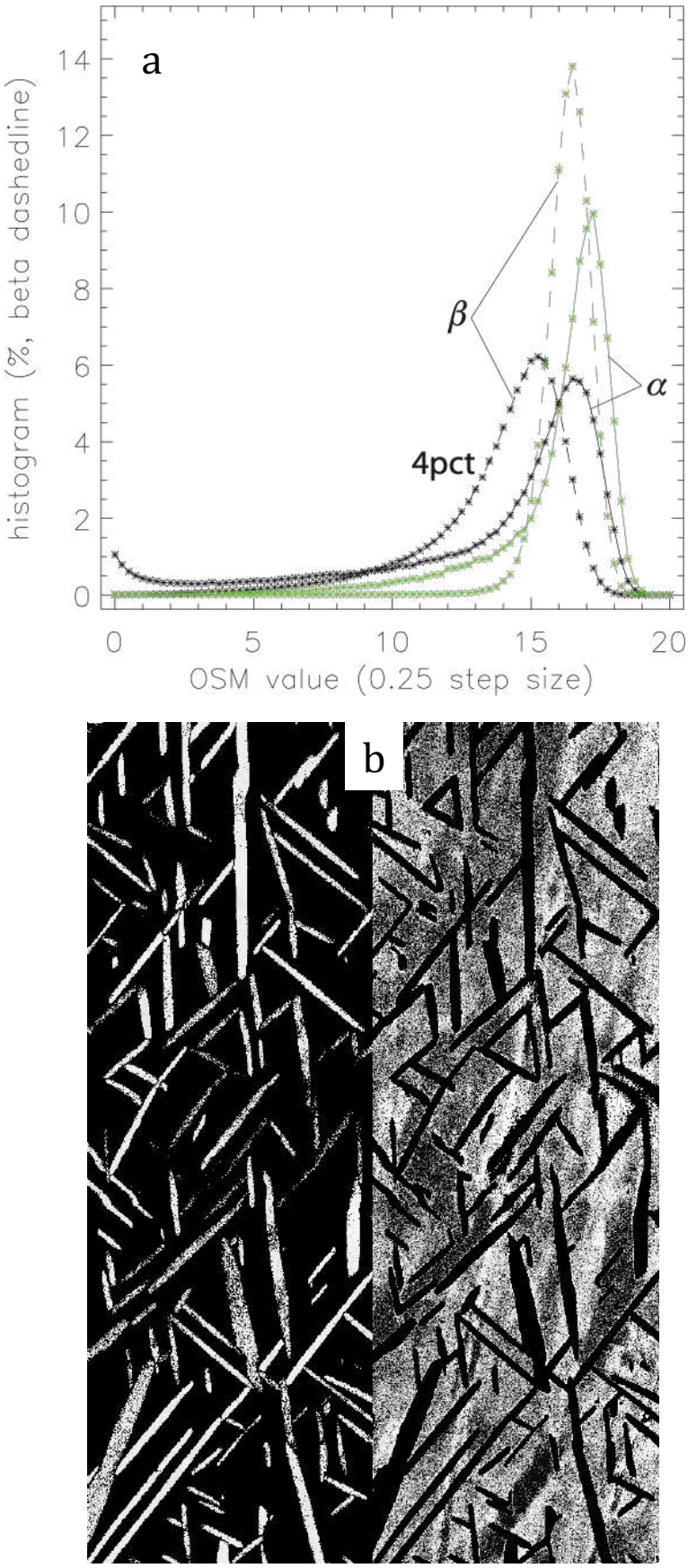

Figure 14: (a) Distribution of an orientation similarity measure obtained from EBSD maps in undeformed β and α phases (green curves) compared to that obtained from samples compressed to about 4% plastic strain. (b) strain partitioning in α and β phases plotted from a measure of the spread of misorientation angles.

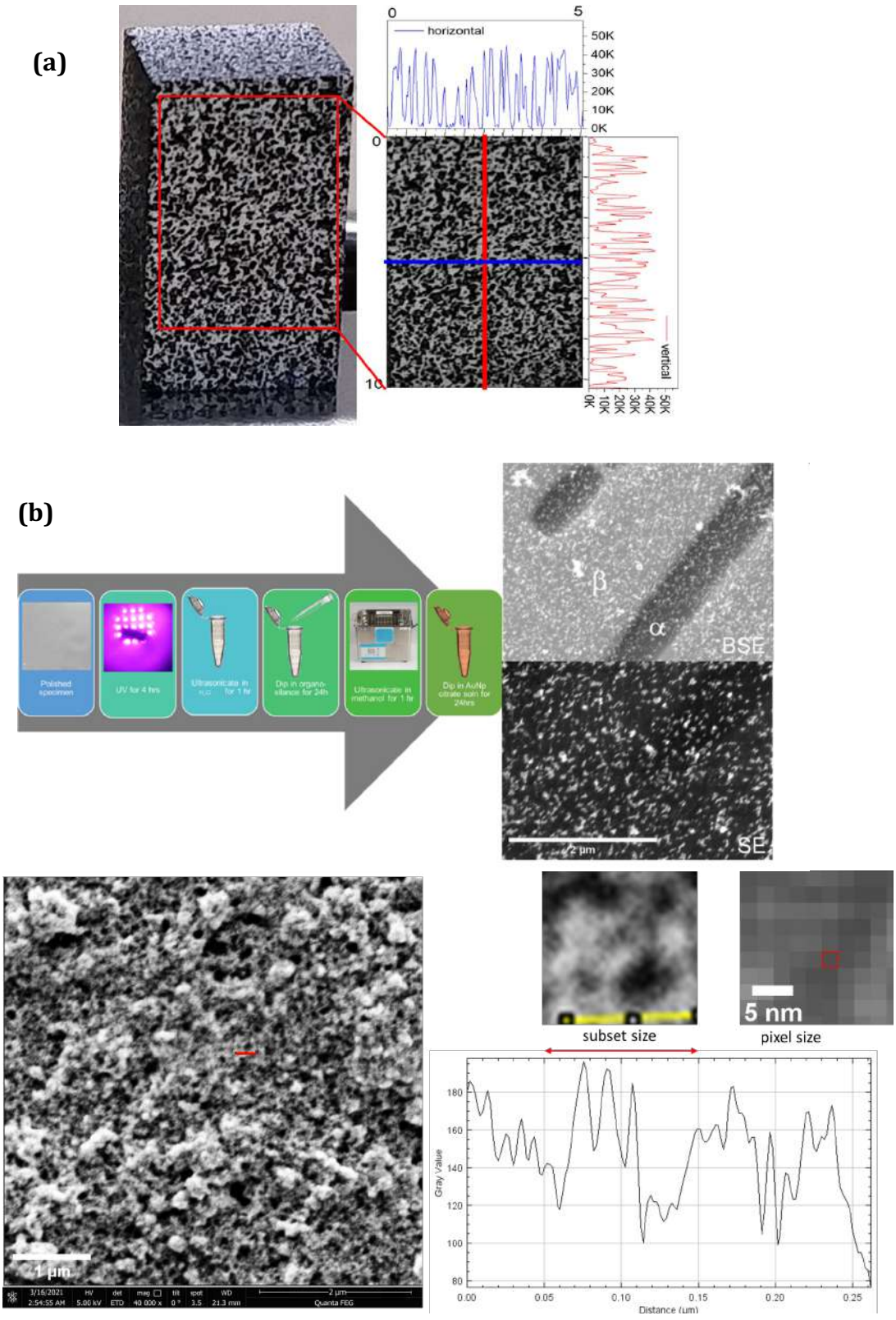

Figure 15: (a) A macro DIC pattern on one face of Ti5553 showing the black-white contrast created by acrylic paint (b) a schematic showing the methodology of steps in Au nanoparticle deposition on Ti5553 with the distribution of Au particles achieved in relation to the underlying structure (c) secondary electron contrast of Au-Ti showing the micro-DIC pattern and the associated intensity profile. An example subset of size 100 x 100 nm and pixel of 2 x 2 nm is also shown.

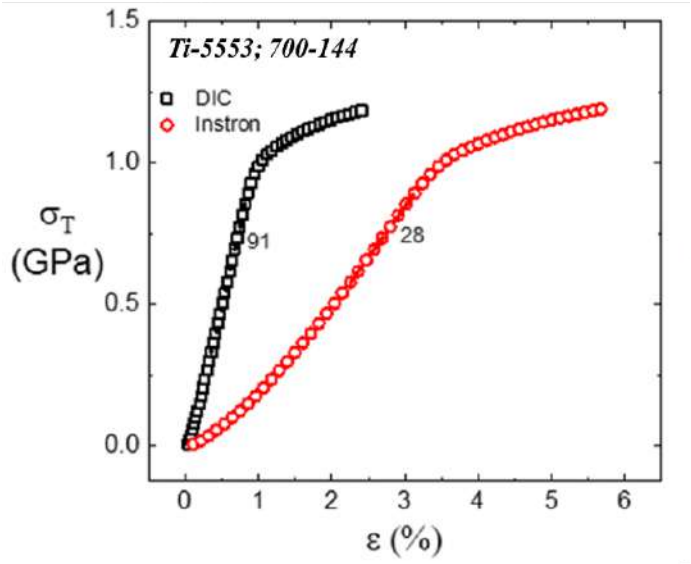

Figure 16: Typical comparative stress-strain curves for Ti5553 700-144 from average pull rod displacement and from average strain in macro-DIC showing elastic and plastic regime

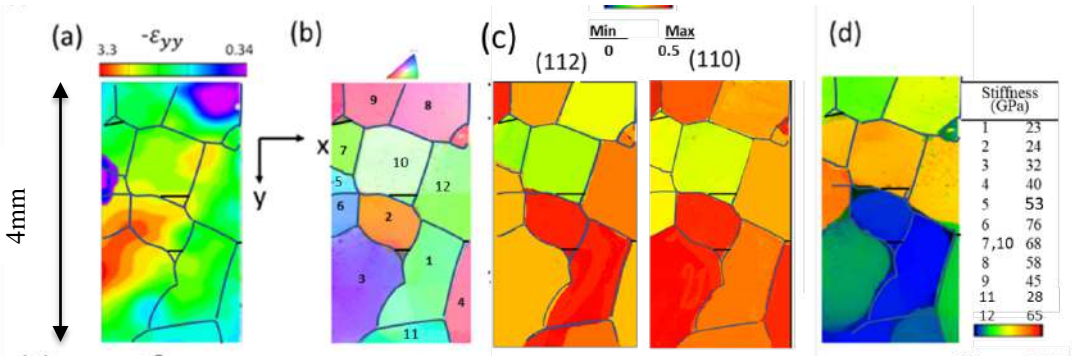

Figure 17: Strain-orientation correlation maps from macro-DIC for the 700-144 sample showing (a) strain map from DIC, (b) corresponding orientation of β grains, (c) Schmidt factor of β phase and (d) the β phase stiffness along the loading direction. The α precipitates within the β grains is not seen at the resolution of these micrographs.

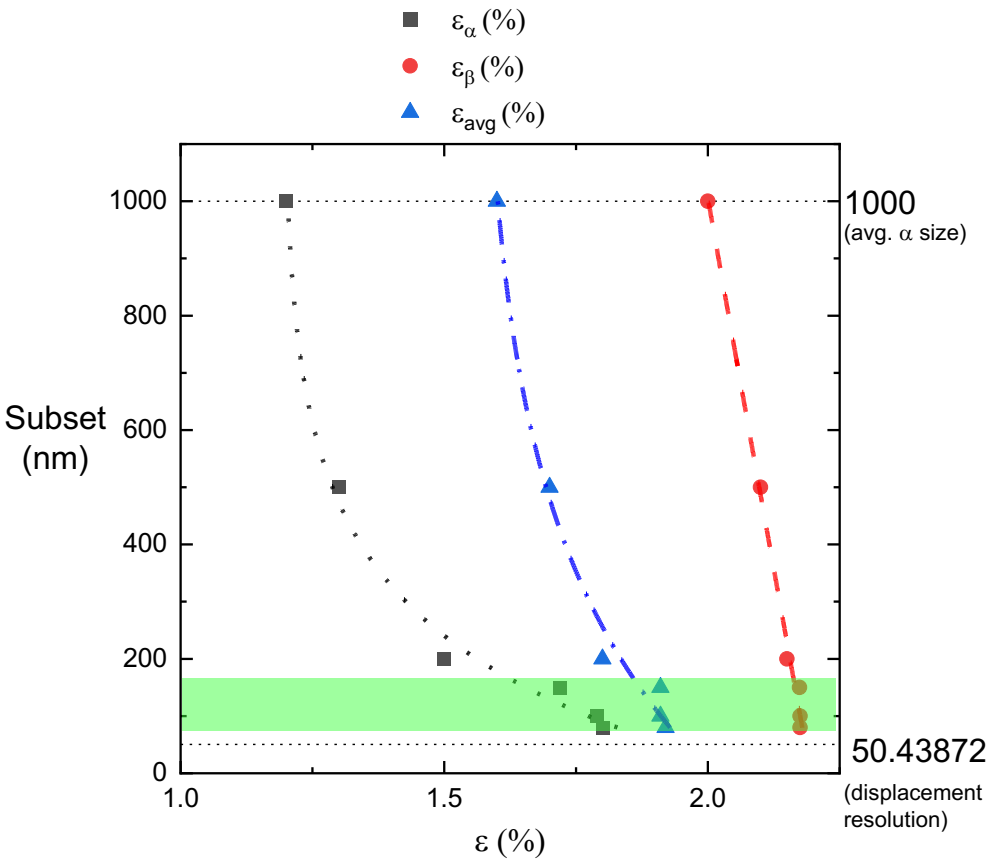

Fig. 18: The effect of subset size on α, β, and average strain for 700-144.

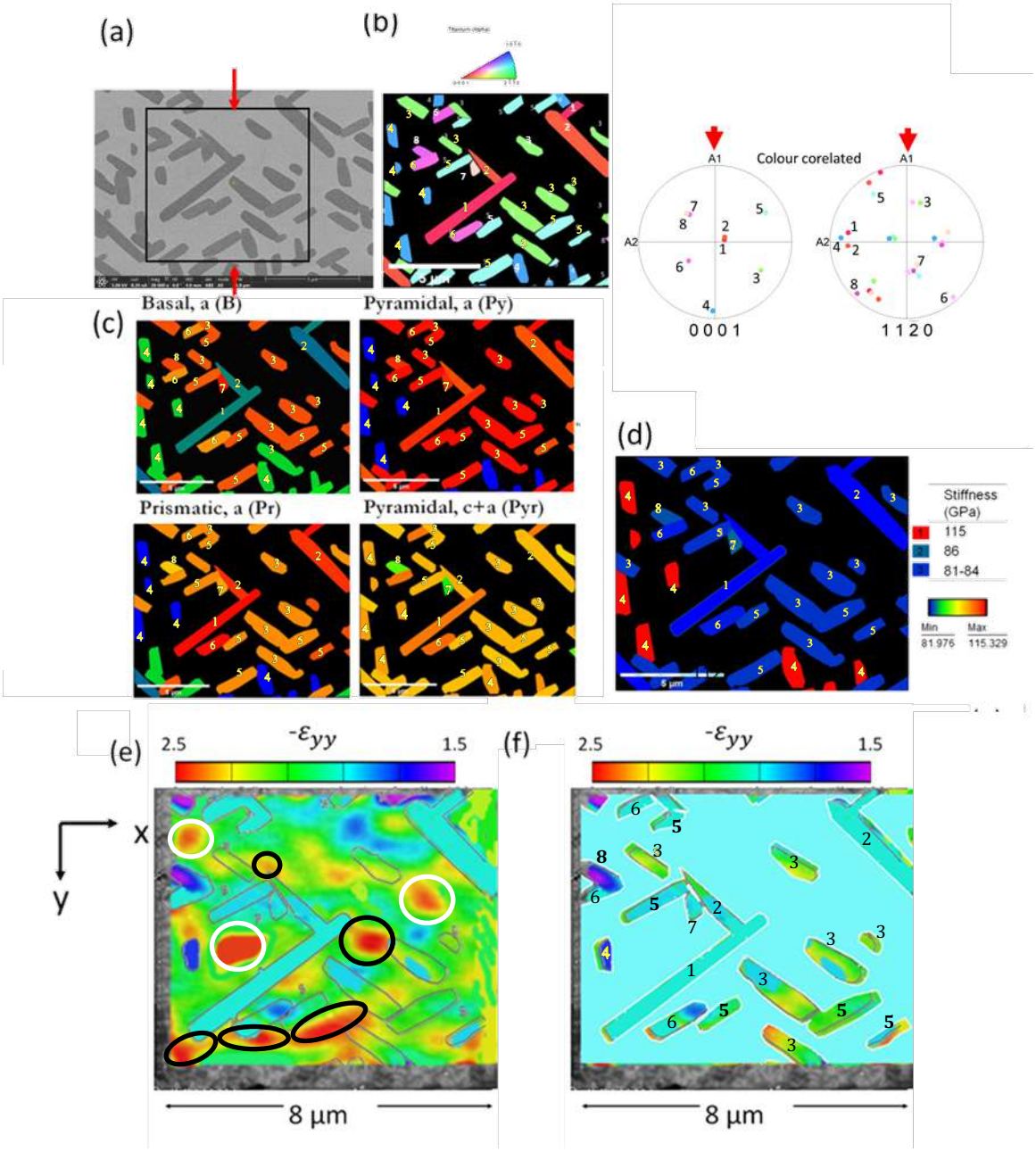

Figure 19: Micro-DIC analysis of Ti5553 for a global plastic strain of 2% for 700-144 showing (a) BSE micrograph of the area of interest, (b) orientation map of α variants (c) Schmid factor of α phase slip systems,(d) modulus of α variants in the loading direction, (e) strain map showing strain in α and β phases, (f) strain map showing strain within α laths

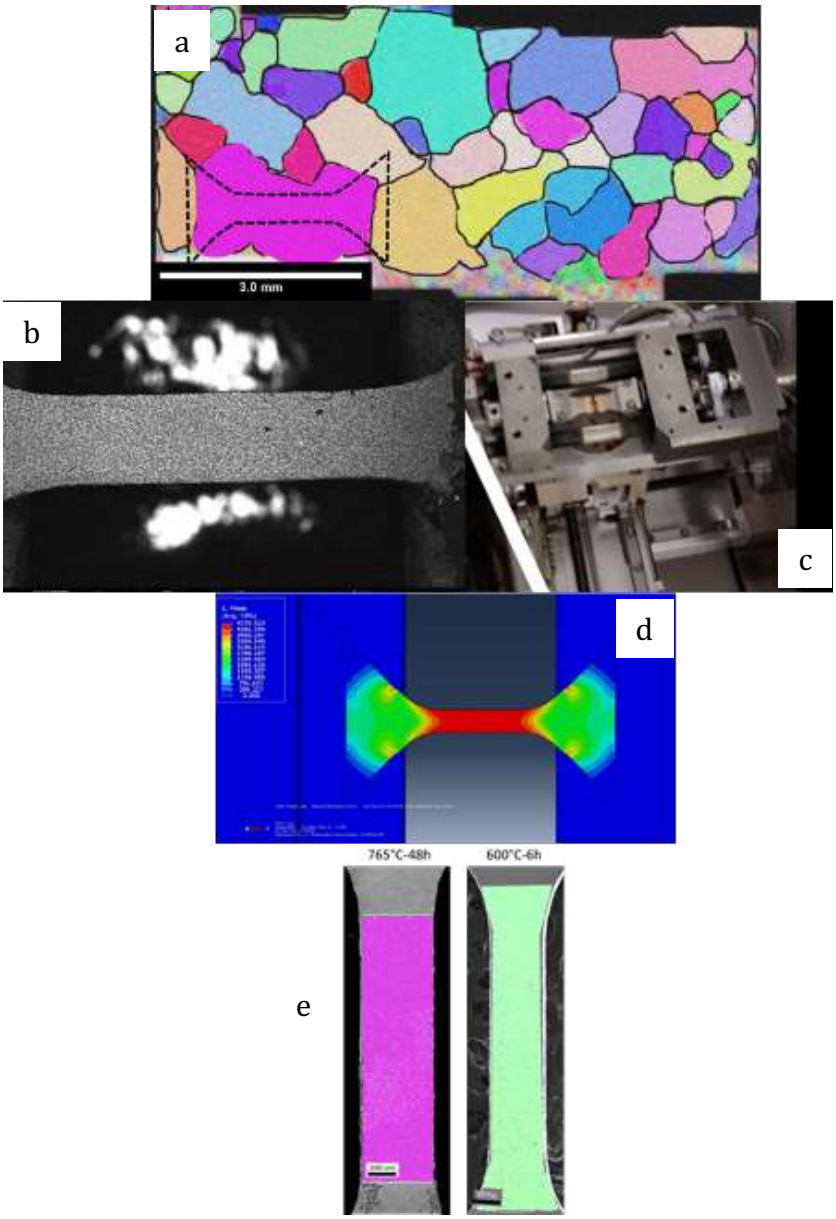

Figure 20: Micro-DIC analysis of Ti5553 showing (a) BSE micrograph of the area of interest with the geometry of the microtensile sample superposed. (b) the DIC speckle on the sample (c) the in-situ tensile test grip with (d) the FEM stress analysis of the sample (e) EBSD patterns on the samples showing single β grains

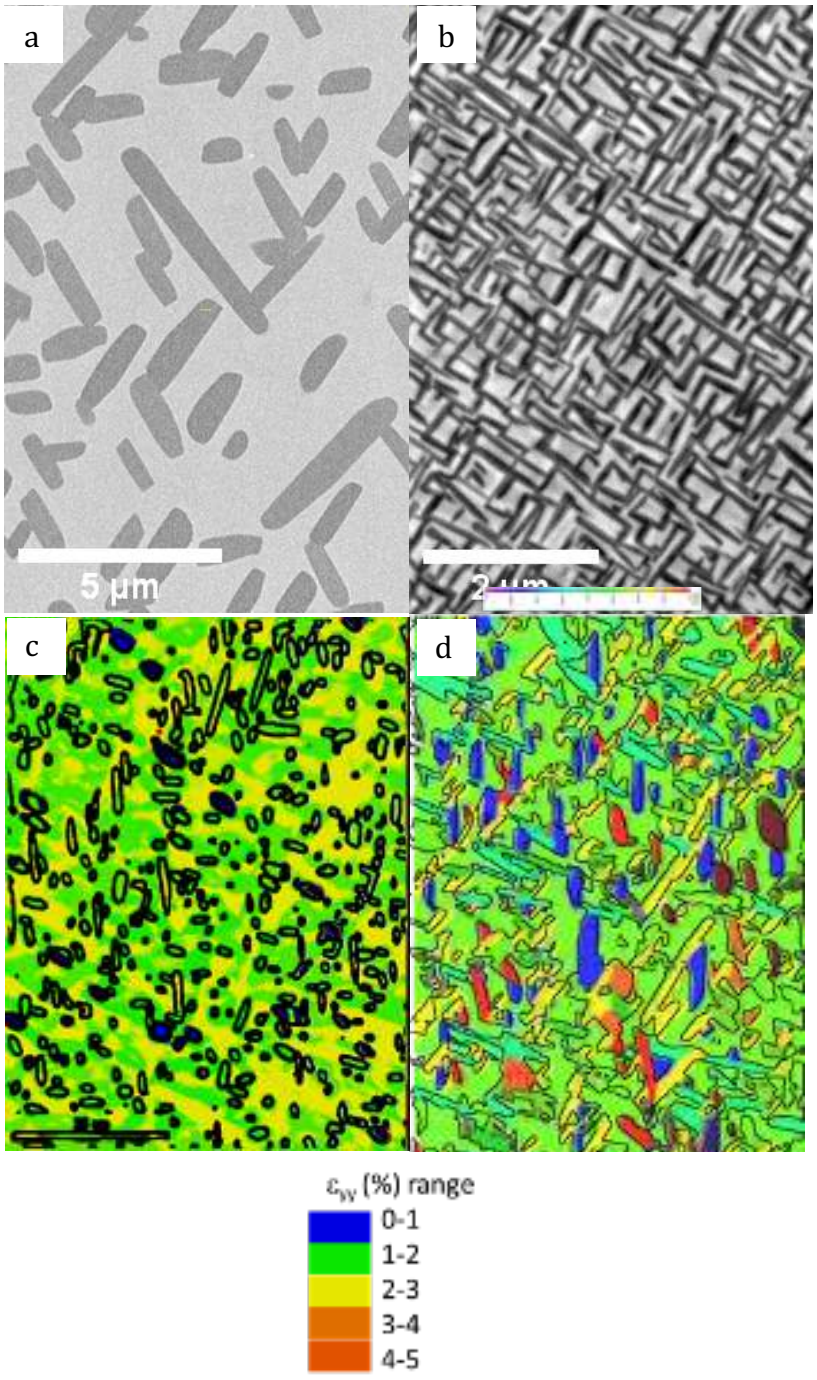

Figure 21: Microstructure of the Ti5553 alloy in backscattered contrast showing different heat treatments of (a) 765°C for 48h (b) 600°C for 6h (c) strain partitioning in the 765°C- 48h sample (d) strain partitioning in the 600°C - 6h sample.

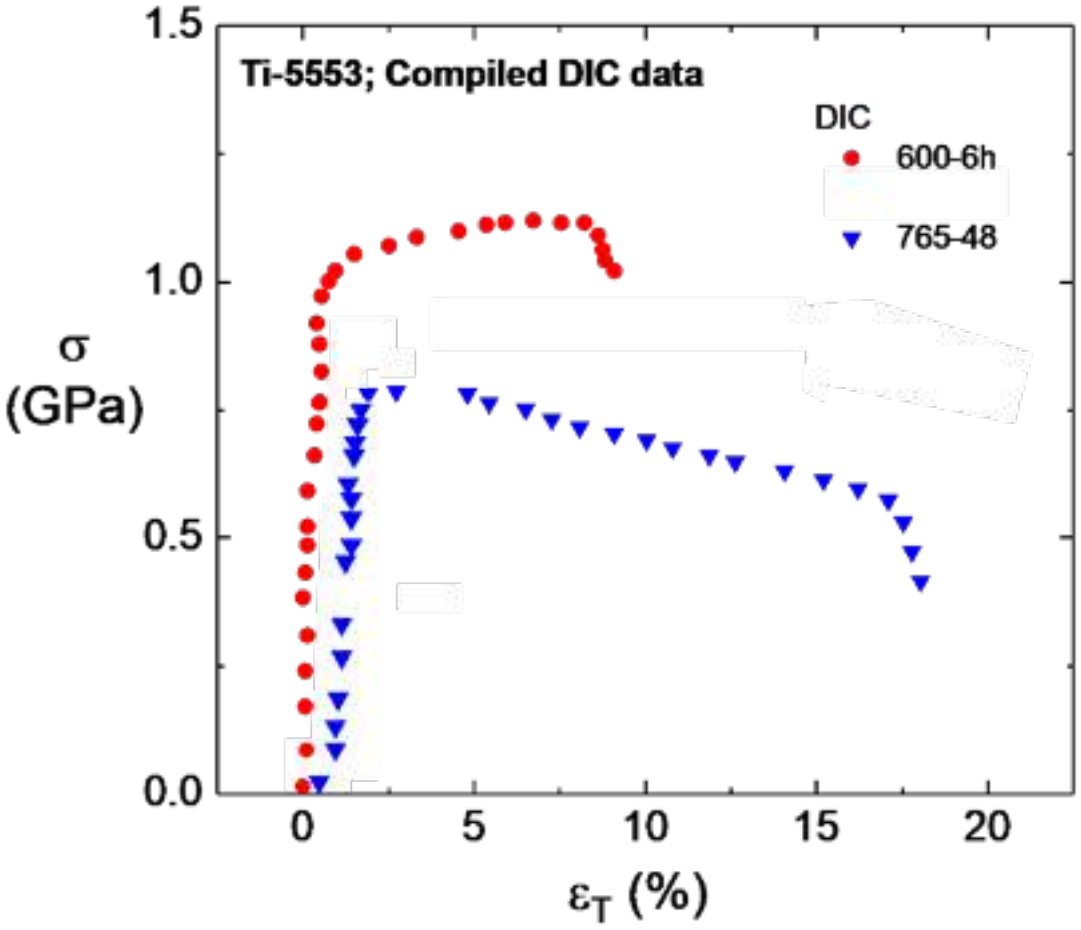

Figure 22: Insitu flow stress curves for the strain partition data shown in Figure 21

4.4 Crystal Plasticity

We have initiated efforts to model strain partitioning with crystal plasticity. We used two dimensional crystal plasticity models in conjunction with experimentally generated sections of EBSD patterns containing real crystallographic non-random variant distribution of the α phase We first explored elastic interactions between the α and β phases and show the strong effect of β phase orientation on the heterogeneities in elastic strain. The EBSD data set was obtained along a <110> zone axis of the β phase and the loading in crystal plasticity simulation was applied along the <100> and <111> directions of the β phase lying in the plane of the section, that is along the soft and hard directions of the β phase. Significant differences in elastic stress distribution are observed along the two orientations, with average von Mises stress in the β phase being higher than in α in the <111> loading direction but lower in the <100> orientation (Figure 23). The effect of the α phase on local stress in β is also evident at the tips of the α plates and along the broad faces for some variants. Increasing the loading into the plastic regime along these orientations resulted in the strain distributions shown Figure 24. At this volume fraction α phase (about 30%), the average strain in β is always greater than the average strain in α in both β loading directions although the difference decreases. in the <111> orientation as might be expected. In addition, strain in α variants depends on their crystallographic orientation. Some features of strain distribution particularly in the <100> orientation can be related broadly to the surface slip observations in Figure 9a and b, in particular the clustering of slip bands and high surface offsets along the broad faces. We show in Figure 24the strain partitioning in a random orientation determined by EBSD of a sample plastically strained to about 4% in compression in comparison with a crystal plasticity simulation in the same orientation along the same loading direction. Although there are some regions of qualitative agreement between the experimental results and simulation as shown by the encircled areas in the β phase, there is significant disagreement as well especially within the α phase variants.

The in situ tests allowed us to calibrate our crystal plasticity parameters with the stress-strain curves for a single α grain. Figure 24 shows the experimental stress-strain curve for the 765°C-48h sample and the crystal plasticity simulation. Figure 24 b and c shows strain partitioning in crystal plasticity and from DIC showing excellent agreement

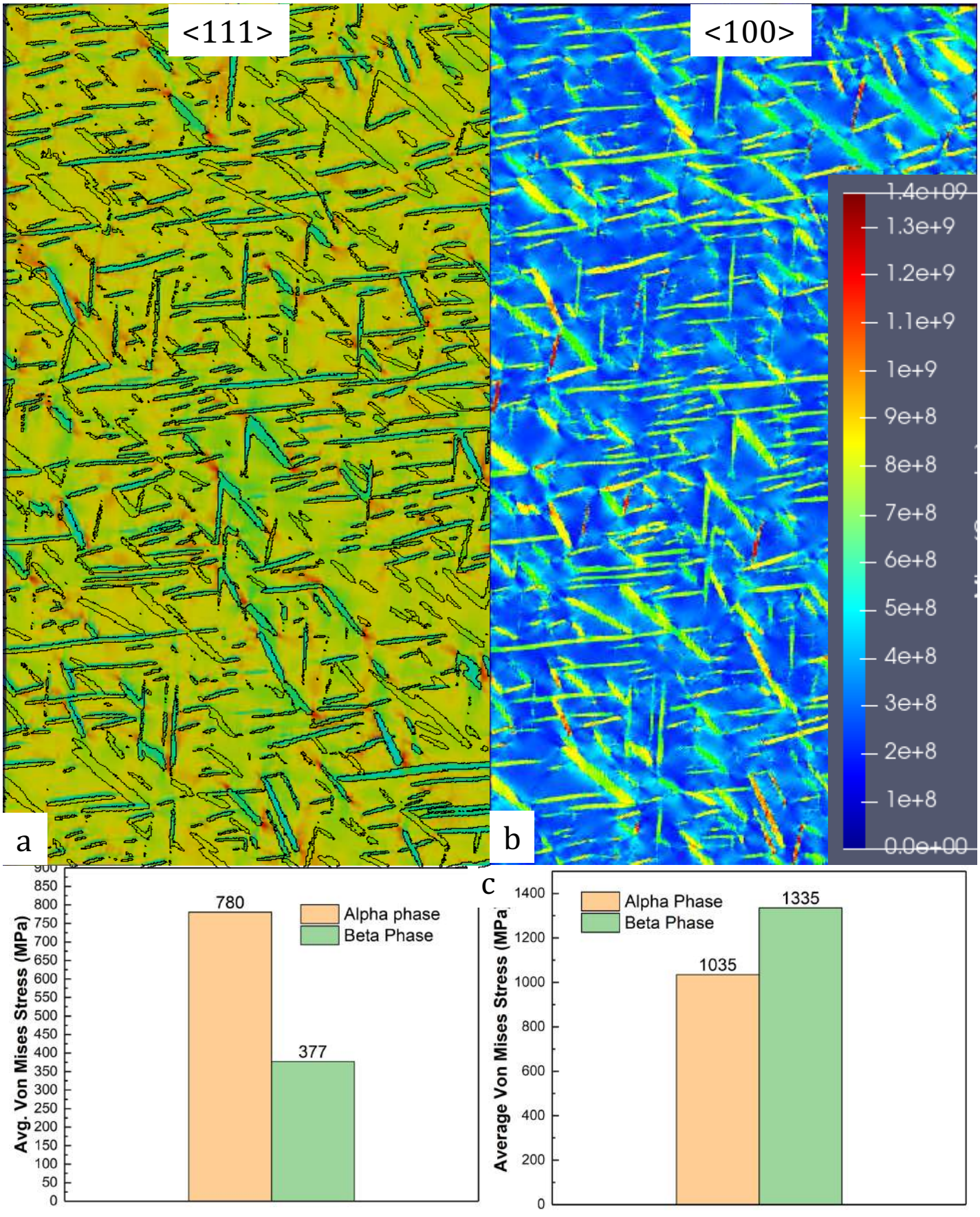

Figure 23: 2d Crystal plasticity simulation of von Mises stress along the loading directions indicated on each figure for a variant distribution obtained by EBSD along a <110> projection. The average Von-Mises stress in each phase is also shown.

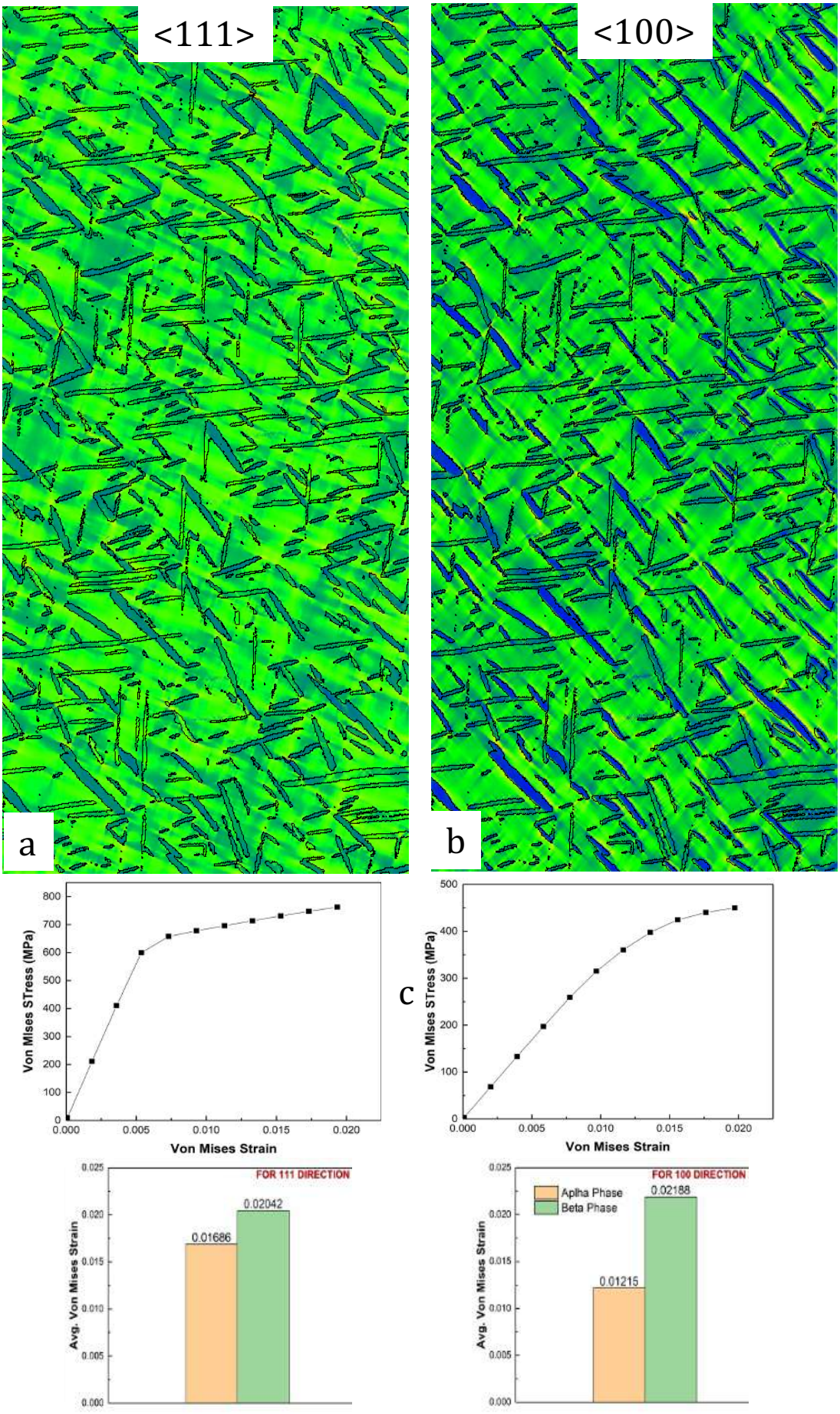

Figure 23: 2d Crystal plasticity simulation of von Mises plastic strain along the loading directions indicated on each figure for a variant distribution obtained by EBSD along a <110> projection. The average von Mises strain in each phase is also shown along with stress-strain curves in each phase.

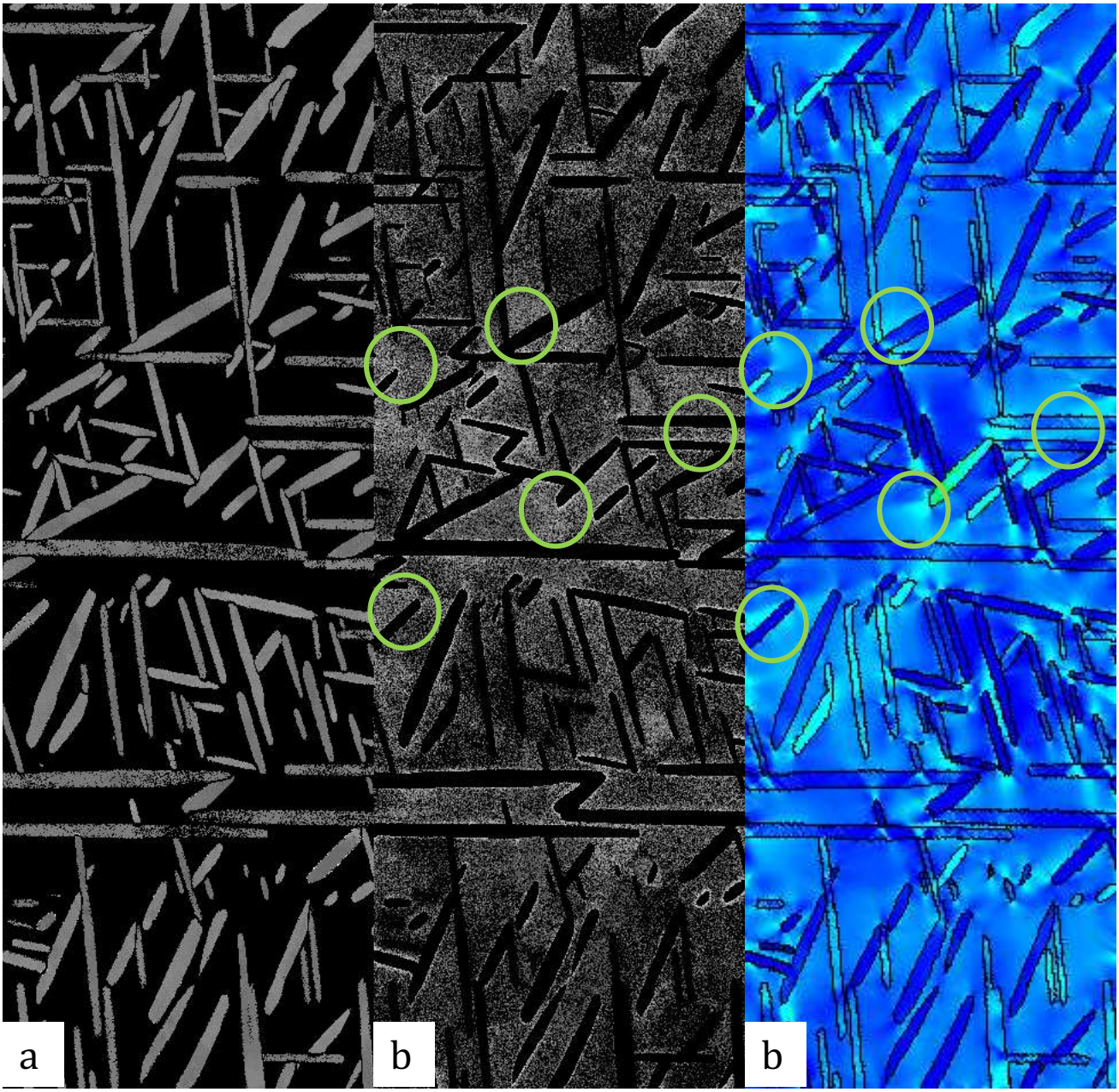

Figure 24: Strain partitioning from a measure of the spread of misorienations angles from EBSD patterns of a sample strained in compression to a plastic strain of about 4% compared with crystal plasticity simulations of the same area along the same loading direction. The encircled regions show qualitative similarities in β phase strain between simulation and experiment

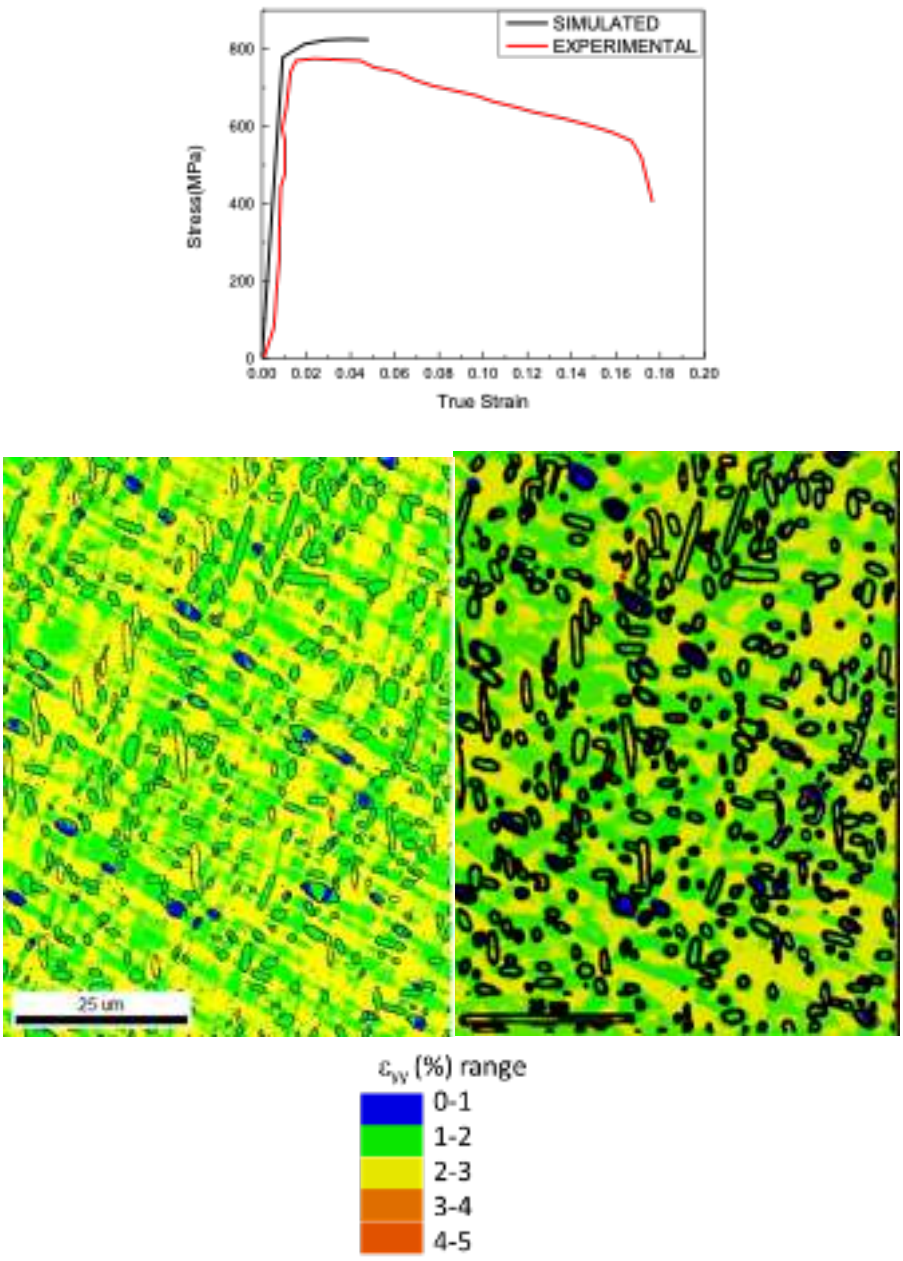

Figure 25: (a) Comparison of crystal plasticity simulated and experimental stress-strain curves for the 765°C-48h in-situ tested sample with a single β grain. (b) Strain partitioning from crystal plasticity simulations of the same area along the same loading direction. (c) Strain partitioning as determined from DIC

5. Summary

1. We have quantitatively determined structural parameters associated with α phase distribution and morphology as a function of heat treatment in the high strength, metastable β alloy Ti 5553.

2. Compression tests had been carried out at room temperature to show the variation of yield strength and work hardening as a function of these structural parameters.

3. Surface slips offsets had been analysed in relation to the scale of the alpha microstructure and it has been shown that slip initiates in the β phase on the {112} <111> system in the form of heterogenous slip bands. Slip lengths are restricted by the interaction of the slip bands with α variants, and therefore depends on the α variant distribution statistics. Yield strength has been shown to scale with slip length and alpha interparticle spacing.

4. Strain partitioning has been examined by both DIC and qualitative EBSD techniques. These experimental results are complemented by initial crystal plasticity simulations of single β grains containing α variant distributions.

5. Future work will refine these crystal plasticity simulations and extend them to polycrystalline β grain structure containing fine scale α phase distributions, and include the effect of α volume fraction and scale. This has not been possible within the current time frames because of Covid induced closures even in the extension period of the project

References

1. Shanoob Balachandran, Ankush Kashiwar, Abhik Choudhury, Dipankar Banerjee, Rongpei Shi, Yunzhi Wang, On variant distribution and coarsening behavior of the α phase in a metastable β titanium alloy, Acta Materialia 106 (2016) 374.

2. S.A. Mantri, D. Choudhuri, A. Behera, J.D. Cotton, N. Kumar, And R. Banerjee, Influence of Fine-Scale Alpha Precipitation on the Mechanical Properties of the Beta Titanium Alloy Beta-21S, Metallurgical And Materials Transactions A , 46A, (2015), 2803.

3. Yufeng Zheng, Robert E.A. Williams, John M. Sosa, Talukder Alam, Yunzhi Wang, Rajarshi Banerjee, Hamish L. Fraser, The indirect influence of the ω phase on the degree of refinement of distributions of the α phase in metastable β-Titanium alloys, Acta Materialia 103 (2016).

4.T.R. Bieler, P. Eisenlohr, C. Zhang, H.J. Phukan, M.A. Crimp, Grain boundaries and interfaces in slip transfer, Current Opinion in Solid State and Materials Science, 18, Issue (2014), 212.

5. R.T. DeHoff, The determination of the size distribution of ellipsoidal particles from measurements made on random plane sections, Trans. Met. Soc. AIME 224 (1962) 474..

6. T. Furuhara, J.M. Howe, H.I. Aaronson, Acta Metall Mater., 39 (1991), 2873.

7. S.A. Saltikov, The determination of the size distribution of particles in an opaque material from a measurement of the size distribution of their sections, in: Stereology, Springer, 1967: pp. 163–173.

8. J. Luster, M. A. Morris, Metall. Mater. Trans., 26A (1995) 1745.

10. A.D. Kammers, S. Daly, Exp. Mech. 53 (2013) 1333–1341.

11. M. Vittoriadiamanti, M.P. Pedeferri, in Nanotechnology in Eco-Efficient Construction: Materials, Processes and Applications, Elsevier Ltd, 2013, pp. 299–326.